CFD Simulations of the AEDC H3 Arc-Jet Flow: Mach 3.3 Nozzle, Flow Surveys, Wedge Models

Tahir Gökçen,[1] Jonathan D. Morgan,[2] Joseph D. Williams,[3] Todd R. White,[4] and Donald T. Ellerby[5]
NASA Ames Research Center, Moffett Field, CA 94035

This paper reports computational simulations and analysis of tests in a high enthalpy arc-jet facility at Arnold Engineering Development Center. These tests were conducted using wedge models placed in a free jet downstream of a 4.5-inch diameter contoured Mach 3.3 nozzle in the H3 facility. For calibration of test conditions, one wedge calibration plate instrumented with an array of pressure and coaxial thermocouple heat flux gages, one stagnation pressure probe and two null-point heat flux calorimeters were used. The pitot pressure and null-point probe measurements give experimental surveys of the test flow, providing assessment of the flow uniformity and valuable data for flow characterization. The present analysis comprises computational fluid dynamics simulations of the nonequilibrium flowfield in the facility nozzle, into the test box and over the wedge models, and comparisons with the experimental measurements. Several issues related to testing are considered: test flow characterization, prediction of surface quantities for three wedge models, effects of model shape change and test article recession, and prediction of surface quantities for the test articles with two circular cavities. These simulations take into account non-uniform total enthalpy profiles at the nozzle inlet as well as the expansion waves emanating from the nozzle exit and their effects on the wedge model flowfields.

I. Nomenclature

c_i	=	mass fraction of species *i*
C_1–C_7	=	heat flux gages on the calibration plate centerline (Fig. 1b)
C_{L1}–C_{L4}	=	heat flux gages on the left side of the calibration plate (Fig. 1b)
C_{R1}–C_{R3}	=	heat flux gages on the right side of the calibration plate (Fig. 1b)
D_e	=	nozzle exit diameter, cm (or in)
h	=	enthalpy, MJ/kg
h_o	=	total enthalpy, MJ/kg
h_{ob}	=	mass-averaged total enthalpy (or bulk enthalpy), MJ/kg
h_{ocl}	=	centerline total enthalpy, MJ/kg
M	=	Mach number
M_e	=	Mach number at the boundary layer edge
$\dot{m}$	=	mass flow rate, kg/s
p	=	pressure, kPa
p_{box}	=	test box pressure, torr
p_{ch}	=	arc-heater pressure, atm
p_o	=	total pressure, atm
p_s	=	surface pressure, kPa
p_{t2}	=	pitot pressure or model stagnation pressure, atm or kPa
p_1, p_2	=	pressure gages on the calibration plate (Fig. 1b)
q_{CWFC}	=	cold-wall full-catalytic heat flux, W/cm^2

[1] Senior Research Scientist, AMA, Inc., Aerothermodynamics Branch, Associate Fellow AIAA
[2] Aerospace Engineer, Thermal Protection Materials Branch, Member AIAA
[3] EDL Systems Engineer, AMA, Inc., Entry System and Vehicle Development Branch, Member AIAA
[4] Senior Research Scientist, Entry System and Vehicle Development Branch, Member AIAA
[5] Senior Research Scientist, Entry System and Vehicle Development Branch

q_{HWFC} = hot-wall full-catalytic heat flux (radiative equilibrium), W/cm^2
q_s = surface heat flux, W/cm^2
Re_x = Reynolds number based on arc length from the nose, $\rho_e u_e s/\mu_e$
Re_θ = Reynolds number based on momentum thickness, $\rho_e u_e \theta/\mu_e$
r_c = wedge or model corner radius, cm
r_n = nose radius, cm
s = arc-length coordinate, m
T = temperature or translational-rotational temperature, K
T_v = vibrational-electronic temperature, K
V = velocity magnitude, m/s
x_{ml} = model location from the nozzle exit plane, cm
δ = boundary layer thickness, mm
ε = hemispherical emissivity, 0.93
μ_e = mixture viscosity at the boundary layer edge, Pa.s
θ = boundary layer momentum thickness, mm
ρ_e = density at the boundary layer edge, kg/m^3
τ_s = surface shear, Pa

II. Introduction

Arc-jets are the primary facilities to study the performance of thermal protection systems (TPS) used on the outer surfaces of spacecraft in an aerothermodynamic heating environment. In a high enthalpy arc-jet facility, a test gas, usually air or a mixture of nitrogen, oxygen and argon, is passed through an electric arc discharge where the energy is added to the flow. The test gas is then expanded through a converging-diverging nozzle into a test chamber to produce high-enthalpy supersonic or hypersonic flow. Arnold Engineering Development Center (AEDC) has three high pressure arc-jet facilities: HEAT-H1, -H2, and -H3 (or the H1, H2, and H3) [1-3]. The H1 and H3 facilities have high-pressure segmented arc heaters, while the H2 facility has a Huels-type arc heater [3]. The NASA Mars Sample Return Earth Entry System TPS (or MSR-EES TPS) project conducted arc-jet tests in the H3 facility in 2023 to evaluate the performance of its baseline forebody TPS, 3-D Woven Mid-Density Carbon Phenolic (3MDCP). In addition, a limited number of Phenolic Impregnated Carbon Ablator (PICA-D) articles were tested. These tests were conducted using wedge models placed in a free jet downstream of the 4.5-inch diameter contoured Mach 3.3 nozzle in the H3 facility. These tests are intended to simulate predicted high shear and heating environments representative of those predicted for the MSR-EES spacecraft heatshield in flight. In addition to the high shear and heating conditions over panel test articles, one important consideration for testing in the H3 facility is the presence of turbulent flow since turbulent flow over the MSR-EES TPS in flight is predicted.

In support of these tests, computational fluid dynamics (CFD) simulations are used to characterize the arc-jet test environment and its parameters consistent with the facility and calibration measurements, and to provide surface quantities (pressure, hot-wall heat flux and shear distributions) as well as other inputs necessary for material thermal response analyses. Other test environment parameters of interest such as boundary-layer thickness, edge Mach number, and Reynolds numbers are estimated. The primary objective of the paper is to report these CFD simulations. The present analysis comprises computational Navier-Stokes simulations of the nonequilibrium flowfield in the facility nozzle, into the test box and over the wedge models, as well as make comparisons of the computational predictions with the calibration plate measurements and probe survey data. Since the wedge models undergo significant shape change during the test, effects of the shape change are assessed with CFD simulations. Also, for the test articles including cavities, CFD simulations are used to predict surface conditions within and downstream of the cavities.

III. Arc-Jet Facility and Tests

The HEAT-H3 facility at AEDC consists of a segmented arc heater, a 70-MW DC power supply, and inter-changeable conical and contoured nozzles, with exit Mach numbers ranging from 1.8 to 3.5 [1-4]. The H3 arc heater produces high-pressure high-temperature air as the test gas (e.g., typically above 100 atm and up to 7500 K) for all nozzles. The H3 facility operates in an atmospheric free jet mode, i.e., the nozzle flow is expanded to the atmospheric test chamber, at total pressures up to 150 atm and inferred total centerline enthalpies up to 20 MJ/kg [2].

(a) 15° wedge calibration model, with 2 pressure and 13 heat flux gages

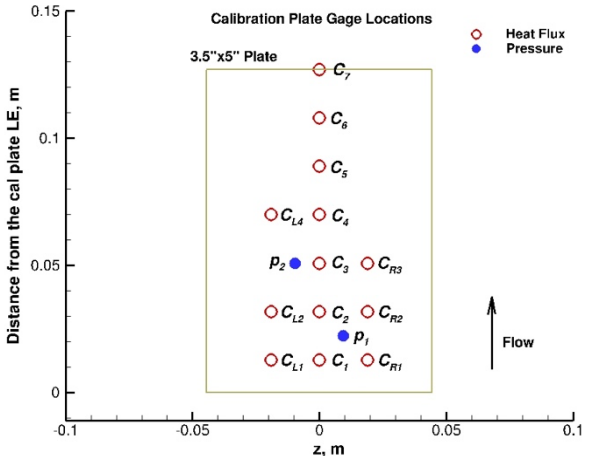

(b) locations of the heat flux and pressure gages on the calibration plate

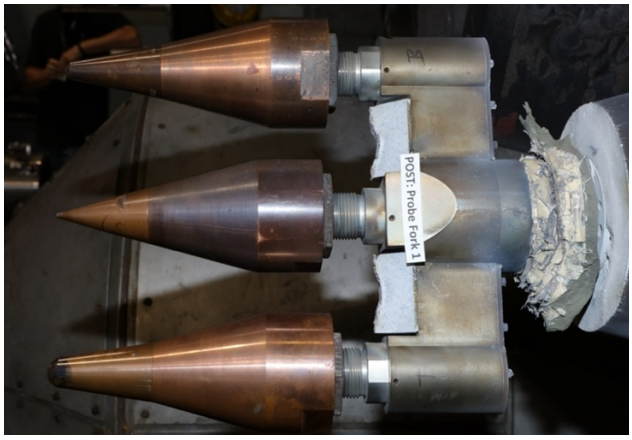

(c) H3 facility fork used for the stagnation pressure and null-point heat flux probe sweeps

(d) 15° one-sided standard TPS wedge model with PICA material

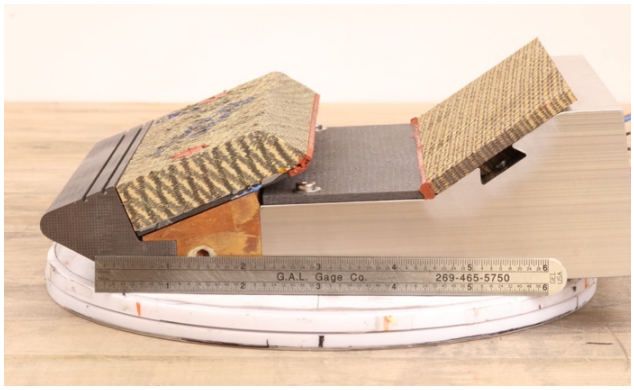

(e) 15° one-sided shoulder feature wedge model with 3MDCP material

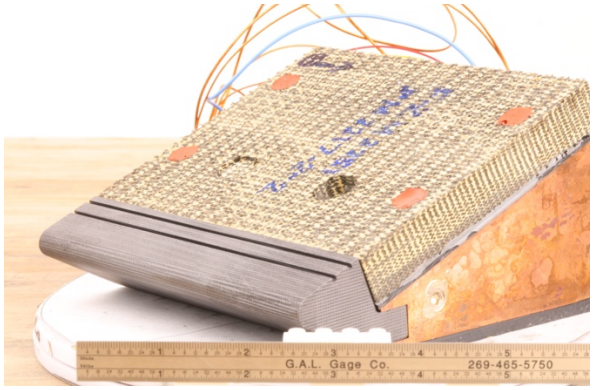

(f) 15° one-sided standard TPS wedge model with 3MDCP material including two circular cavities

Figure 1. Photographs of the wedge calibration model, calibration plate gage locations, stagnation probes, and examples of three TPS wedge models used in the H3 Mach 3.3 nozzle tests (H3-048, Run 2).

The MSR-EES TPS tests (H3-048) were conducted using wedge models placed in a free jet, 0.254 cm (0.1 in) downstream of the 4.5-inch diameter contoured Mach 3.3 nozzle in the H3 facility. For calibration of test conditions, the following facility-provided calorimeter models were used: one 15° calibration wedge model that has a plate instrumented with an array of pressure and coaxial thermocouple heat flux gages, one stagnation pressure probe, and

two different sized null-point heat flux calorimeters [4, 5]. Two new one-sided TPS wedge models were used to accommodate panel test articles in the H3-048 tests (2023): a 15° standard wedge model and a 15° shoulder feature wedge model. Both wedge models were designed by Joseph Williams to increase panel thickness over those used in the previous HEEET tests [6, 7]. The new test panel thickness can be up to 1.94 cm, which is comparable to the estimated MSR-EES TPS thickness. The feature wedge model is a shorter version of the standard TPS wedge model, but it includes a shoulder feature like the MSR-EES TPS shoulder geometry. Note that although all wedge models have the same 15° inclination angle, there are differences in their geometries. The calibration wedge model has a nose radius of 0.381 cm (0.15 in) and a width of 9.2 cm while both TPS wedge models have 0.508 cm (0.2 in) nose radius and 13.82 cm width. The plate leading edge locations, with respect to the nose, are different between the calibration wedge and TPS wedge models. There were also test articles with two circular cavities used with the standard TPS wedge model. These cavities, with differing depths, were intended to simulate potential TPS damage for the limiting cases (closed and open cavities).

Figure 1 shows photographs of the wedge calibration model, calibration plate gage locations, stagnation probes, and examples of three 15° TPS wedge models used in the H3-048 arc-jet tests. The two pressure ports and thirteen heat flux gage locations of the calibration plate are given in Fig. 1b and are also seen in the photograph shown in Fig. 1a. The axial spacing between the centerline heat flux gages is 1.91 cm (0.75 in), which is also the spacing between the centerline and off-centerline heat flux gages at the same streamwise location. The probe fork shown in Fig. 1c includes one stagnation pressure probe and two null-point stagnation calorimeters (0.635-cm and 0.953-cm nose radii), and it produces three survey profiles when swept through the test flow. These experimental surveys of test flow provide assessment of the flow uniformity and valuable data for flow characterization. Details of these calibration models can be found in [4]. Also shown in Fig. 1 are pretest photographs of the standard TPS wedge model with PICA material, the shoulder wedge model with 3MDCP material, and the standard TPS wedge model with 3MDCP material including two circular cavities. Note that each wedge model has small grooves (~1.5 to 1.6 mm wide) just upstream of its plate leading edge to promote the transition to turbulent flow. Further details of the H3-048 tests and test articles are reported in a companion paper [8]. A summary of the AEDC H3 facility parameters, wedge calibration plate and stagnation probe data for H3-048 tests is given in Table 1.

IV. Computational Approach

Computational analyses of arc-jet tests are performed through simulation of nonequilibrium expanding flow in the arc-jet nozzle and supersonic jet, and simulation of the flow in the test box and around the test articles. For all CFD calculations, the Data Parallel Line Relaxation (DPLR) code [9, 10], a NASA Ames in-house flow solver, is used. DPLR provides various options for thermophysical models and formulation. For CFD calculations presented here, two-dimensional axisymmetric or three-dimensional Navier-Stokes equations, supplemented with the equations accounting for nonequilibrium kinetic processes, are used in the formulation. The thermochemical model employed for the arc-jet flow includes five species (N_2 O_2, NO, N, O), or six species (N_2 O_2, NO, N, O, Ar) when argon is present, and the thermal state of the gas is described by two temperatures (translational-rotational and vibrational-electronic) within the framework of Park's two-temperature model [11].

The flowfield in an arc-jet facility, from the arc heater to the test section, is a very complex, three-dimensional flow with various nonequilibrium processes occurring. To simulate the arc-jet facility flowfield, several simplifying assumptions are made, and corresponding numerical boundary conditions are prescribed for CFD simulations. The present computational approach follows our earlier work [12-16], and it is also briefly described here. Simulations of the arc-jet facility flow are started from the nozzle inlet. The total enthalpy and its radial profile at the inlet are prescribed based on the facility and calibration data, and the flow properties at the inlet are assumed to be in thermochemical equilibrium. Measured facility data, namely the total pressure, mass flow rate, and test box pressure, are used as boundary conditions. All metallic surfaces, water-cooled nozzle walls, and calorimeter model and calibration plate surfaces are assumed to be fully catalytic to recombination reactions of atomic oxygen and nitrogen at a constant temperature of 500 K. The hot-wall heat flux and surface temperatures are calculated using the radiative equilibrium boundary condition ($\varepsilon = 0.93$). For all cases, the turbulent simulations are performed using the one-equation model of Spalart-Allmaras [17, 18] with Catris and Aupoix modifications [19] (SA model, SA1001 in DPLR). For comparison purposes, limited turbulent simulations are also performed using the two-equation Shear Stress Transport (SST) model of Menter [20] with a compressibility correction (SST model, SST2003 in DPLR or SSTc2 in [21]), and the algebraic model of Baldwin-Lomax [22] (BL model). Implementations of these turbulence models in DPLR and their applications are described by Brown [21, 23].

Table 1. A summary of the AEDC H3 facility parameters, wedge calibration plate data, and stagnation probe data for H3-048 tests.

Test Run/Facility Data	Run 1	Run 2	Run 3
p_{ch}, atm	104–105	103–104	104–105
p_{box}, torr	760	760	760
$\dot{m}$, kg/s	5.51	5.49	5.50
h_{ob}, MJ/kg	6.1– 6.7	6.1– 6.7	6.1– 6.6
Wedge calibration plate	**Sweep 1**	**Sweep 1/Sweep 3**	**Sweep 3/Sweep 4**
p_1, p_2, kPa	296, 278	304, 288	303, 283
		300, 279	297, 276
C_{L1}, C_{L2}, C_{L4}, W/cm^2	980, 765, _	1087, –, 689	979, 870, 792
		1258, –, 850	1031, –, 805
C_1, C_2, C_3, C_4, C_5, C_6, C_7	1246, 1130, –, 932, 762, 814, 726	1377, 1194, –, 1094, 830, 834, 788	1328, 1193, –, 1016, 805, 851, 734
		–, 1186, –, 1079, 840, 870, 812	–, 1074, –, 1367, 747, 802, 711
C_{R1}, C_{R2}, C_{R3}	1153, –, 1016	1239, –, 1069	1232, –, –
		1058, –, 883	1135, –, –
H3 facility stagnation probes	**Sweep 2**	**Sweep 2/Sweep 4**	
q_{NP} (r_n = 0.635 cm), W/cm^2	5760–6730	5640–7030	
		6140–7180	
q_{NP} (r_n = 0.953 cm)	5650–6620	5460–6080	
		5870–6150	
p_{t2}, atm	13.2–14.1	13.6–14.9	
		13.5–14.6	

h_{ob} is the AEDC facility estimate of the bulk enthalpy, which is determined by the energy balance method [24].
The axial spacing between the centerline calorimeters on the calibration plate and the spacing between the centerline and off-centerline calorimeters are 1.91 cm.

Table 2. A summary of CFD facility parameters and estimates of plate surface quantities on the 15° calibration wedge and two one-sided TPS wedge models, x_{ml} = 0.254 cm.

H3-048 Facility/Test Parameters	CFD Estimates
p_o, atm	104
p_{box}, torr	760
$\dot{m}$, kg/s	5.49
h_{ob}, MJ/kg	7.1
h_{ocl}, MJ/kg	9.9
Stagnation probes, centerline	
q_{NP} (r_n = 0.635 cm), W/cm^2	6254
p_{t2}, atm	13.85
Calibration wedge model	
p_s, kPa	288 – 195
q_{CWFC}, W/cm^2	1350 – 955
τ_s, Pa	2672 – 2174
δ, mm	0.41 – 2.11
M_e	1.61 – 1.85
Re_x	$7.8\text{x}10^4$ – $5.6\text{x}10^5$
Re_θ	281 – 1183
Standard TPS wedge model	
p_s, kPa	291 – 197
q_{HWFC}, W/cm^2	783 – 599
τ_s, Pa	2531 – 2160
δ, mm	0.66 – 2.21
M_e	1.59 – 1.81
Re_x	$1.2\text{x}10^5$ – $4.5\text{x}10^5$
Re_θ	337 – 893
Shoulder feature wedge model	
p_s, kPa	291 – 277
q_{HWFC}, W/cm^2	784 – 734
τ_s, Pa	2538 – 2318
τ_s (max at the shoulder), Pa	4329
δ, mm	0.66 – 1.65
M_e	1.59 – 1.61
Re_x	$1.2\text{x}10^5$ – $3.1\text{x}10^5$
Re_θ	337 – 809

h_{ob} is the mass-averaged total enthalpy at the nozzle inlet using a parabolic enthalpy profile at constant pressure.
The ranges of CFD estimates are given along the plate centerline, all starting from the plate leading edge to 12.7 cm, 10.2 cm, and 5.0 cm downstream for the calibration, standard TPS, and shoulder feature wedge models, respectively.

The stagnation probe sweep data of H3-048 tests, obtained with the pitot pressure and two null-point heat flux probes shown in Fig. 1c, indicate that the flow exiting the H3 Mach 3.3 nozzle is not uniform. Characterization of this non-uniformity in CFD simulations is very important, especially considering the widths of the wedge models tested are comparable to or even larger than the nozzle exit diameter. Any non-uniformity in enthalpy directly affects model

surface conditions and their distributions. The total enthalpy profile used at the nozzle inlet in the CFD simulations is determined such that the probe survey data can be reproduced with CFD simulations. The approach for analysis of the probe sweep data and comparisons with CFD simulations follows the approach presented in [15], and references therein. While the data obtained from the pitot pressure surveys are used as quantitative data, the null-point gage heat flux measurements from the probe surveys are used qualitatively. Therefore, only normalized distributions of the heat flux measured by the survey probes are used in comparisons with computations to estimate the centerline-to-bulk enthalpy ratio, h_{ocl}/h_{ob}. Also, all probe sweep data comparisons are made based on computed axisymmetric CFD flowfields. For quantitative pitot pressure comparisons, computations are based on the CFD flowfield and shock relations (pressure, Mach number, frozen flow). For normalized heating distribution comparisons, the heat flux from the null-point heat flux probes is assumed to be proportional to $h_o p_{t2}^{1/2}$, and corresponding computations are based on the CFD flowfield.

V. Presentation of Results

First, comparisons of CFD simulations with the pitot pressure and heat flux survey data are presented. Second, the 15° calibration wedge model simulations are given, including comparisons with the calibration plate data. Third, the simulation results for the two one-sided TPS wedge models will follow. Then, effects of the model shape change are assessed for one case with CFD simulations using an idealized recessed geometry for the shoulder feature wedge model. The considered effects include the changes in flowfield features and model surface quantities. Finally, CFD simulation results are presented for the wedge plate with the two circular cavities (closed and open).

A summary of CFD facility parameters and estimates of plate surface quantities on the calibration wedge and two TPS wedge models is given in Table 2.

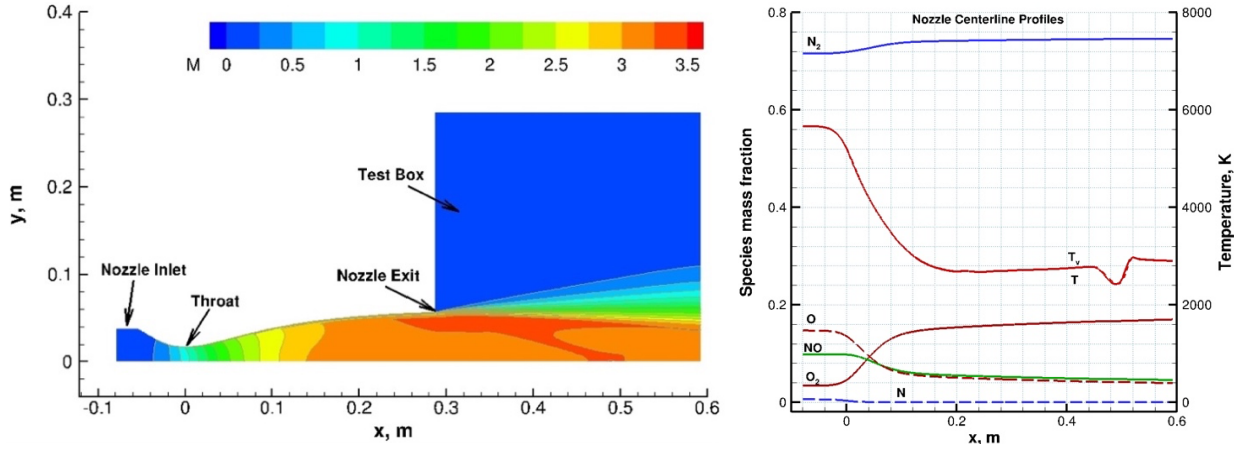

(a) Mach number **(b) flow properties**

Figure 2. Computed Mach number contours of the nozzle flow including the test box, and selected flow properties along the nozzle centerline. Axisymmetric simulation of the H3 Mach 3.3 nozzle flow: $\dot{m}$ = 5.49 kg/s, h_{ob} = 7.1 MJ/kg, h_{ocl} = 9.9 MJ/kg, parabolic enthalpy profile, p_{box} = 760 torr, turbulent flow (SA model).

A. Flow characterization: comparisons with pitot pressure and null-point heat flux survey data

As a typical axisymmetric simulation, Fig. 2 shows a computed H3 Mach 3.3 nozzle flowfield including the test box and selected flow properties along the nozzle centerline. In Fig. 2a, computed Mach number contours are shown. The expansion waves emanating from the nozzle lip to the test box and the shear layer are clearly seen. To provide some insight into the nonequilibrium flowfield chemistry within the nozzle, species mass fraction and temperature profiles along the nozzle centerline are shown in Fig. 2b. Starting with partially dissociated nitrogen and oxygen at the nozzle inlet, the flow goes through a nonequilibrium expansion process in the converging-diverging nozzle. During this expansion process, most of the dissociated N atoms recombine to N_2 or form NO, but at the nozzle exit, partially dissociated oxygen and NO remain. At this relatively high pressure and moderately high enthalpy level, the computations predict that the flow remains in thermal equilibrium. The dip in the temperature profiles in the test box

at about x=0.5 m is a result of the expansion waves generated at the nozzle exit reaching the nozzle/test box centerline and the following reflection downstream. Also, since there is a non-uniform enthalpy profile at the inlet, which is not shown here but will be discussed shortly, flow properties and composition vary significantly at the nozzle exit.

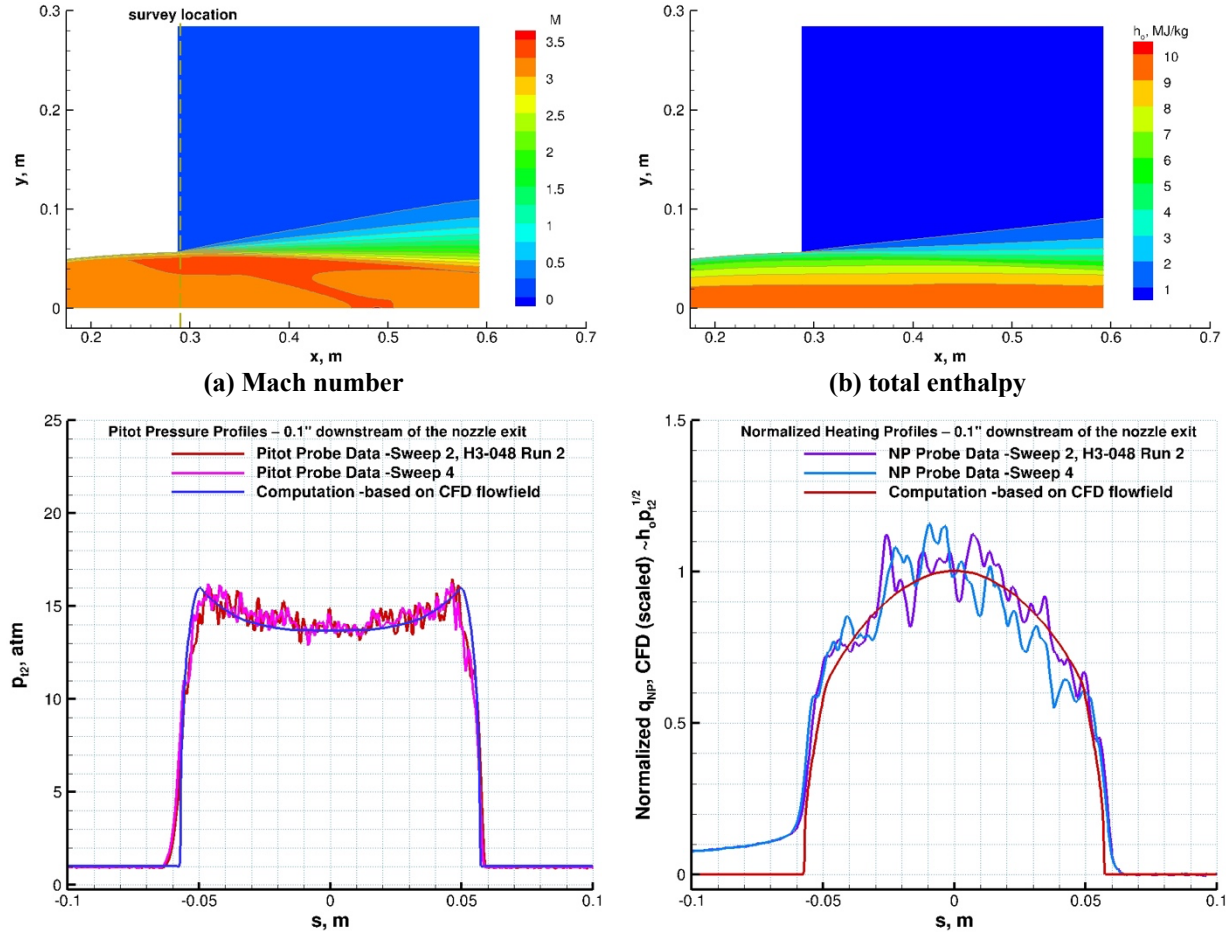

Figure 3. Computed Mach number and total enthalpy contours of the nozzle flow and test box, and comparisons of computations with the pitot pressure and heat flux survey data at x_{ml} = 0.254 cm location (0.635-cm radius null-point probe). Axisymmetric simulation of the H3 Mach 3.3 nozzle flow: $\dot{m}$ = 5.49 kg/s, h_{ob} = 7.1 MJ/kg, h_{ocl} = 9.9 MJ/kg, parabolic enthalpy profile, p_{box} = 760 torr, turbulent flow (SA model).

Figure 3 shows the computed Mach number and total enthalpy flowfield contours near the exit of the H3 Mach 3.3 nozzle and test box, and comparisons of computations with the pitot pressure and heat flux survey data at x_{ml} = 0.254 cm location. Since the Mach 3.3 nozzle is a contoured nozzle, the computed Mach numbers at the nozzle exit are relatively uniform (Fig. 3a). The heat flux data were obtained using the 0.635-cm radius null-point probe. These surveys, taken very close to the nozzle exit (only 0.25 cm downstream, Fig. 3a), clearly show that the test flow exiting the nozzle is non-uniform. Effects of the shear layer and expansion waves on the sweep data are relatively small. Note that both pitot pressure and heat flux sweep data are reasonably repeatable within the measurement fluctuations in the two sweep directions (Sweep 2 and Sweep 4), although the variations in the heat flux data are much larger than those in the pitot pressure data. These probe sweeps are used to set the inlet boundary conditions used in CFD simulations that use non-uniform total enthalpy and mass flux profiles, following our earlier work (e.g., see [15]). For the CFD simulations shown in Fig. 3, a parabolic total enthalpy profile and uniform pressure at the inlet are prescribed, reproducing the measured survey data reasonably well. For this case, the estimated centerline-to-bulk enthalpy ratio, h_{ocl}/h_{ob}, is 1.39.

As mentioned earlier, two null-point heat flux probes were used. Figure 4 shows the measured heat flux data using these two null-point probes. The sweep data obtained with both probes are reasonably consistent within the

measurement fluctuations in both sweep directions (Sweep 2 and Sweep 4). The 0.635-cm probe data is higher than the 0.953-cm probe data as expected, but it is not as high as the theoretical value of 22.5%. In any case, both probe data clearly show that the flow is not uniform.

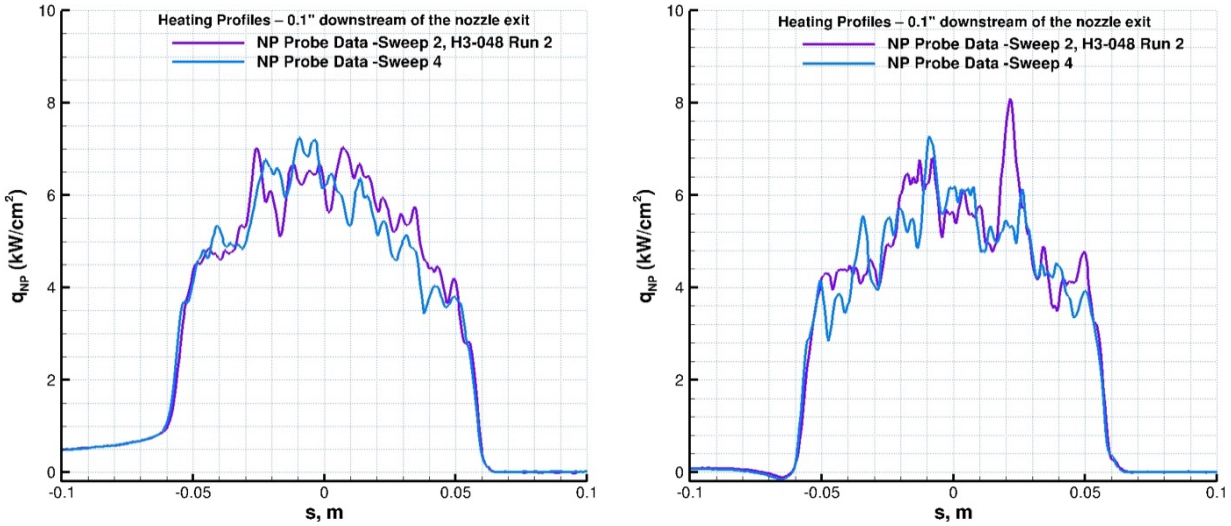

(a) 0.635-cm radius null-point probe **(b) 0.953-cm radius null-point probe**

Figure 4. The heat flux survey data obtained with the two null-point probes at x_{ml} = 0.254 cm location during H3-048 tests Run 2.

B. H3 Mach 3.3 nozzle flow and 15° calibration wedge model simulations

In this section, three-dimensional simulations of the nozzle and test box flowfield are presented first, and then the 15° calibration wedge model simulations including comparisons with the calibration plate pressure and heat flux data will follow.

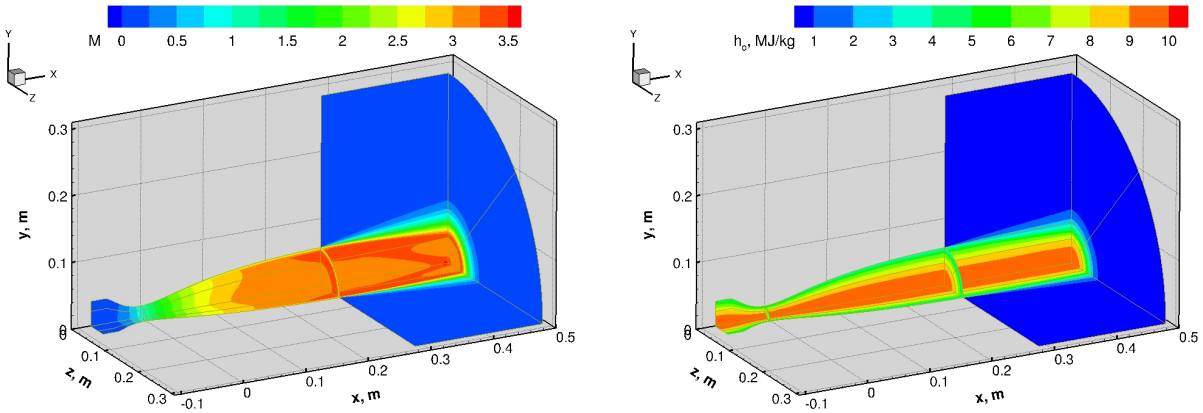

(a) Mach number **(b) total enthalpy**

Figure 5. Computed flowfield Mach number and total enthalpy contours of the H3 Mach 3.3 nozzle and test box. $\dot{m}$ = 5.49 kg/s, h_{ob} = 7.1 MJ/kg, h_{ocl} = 9.9 MJ/kg, parabolic enthalpy profile, p_{box} = 760 torr, turbulent flow (SA model).

Figure 5 shows the computed flowfield Mach number and total enthalpy contours of the H3 Mach 3.3 nozzle and test box. The contours are shown on the *x*-*y* and *x*-*z* planes of the nozzle/test box flowfield (symmetry planes) and on three *y*-*z* planes: one at the nozzle throat, one at the nozzle exit, and another at the test box exit.

Figure 6 shows the computed Mach number and total enthalpy contours of the H3 Mach 3.3 nozzle flow near the nozzle exit and test box with the 15° calibration wedge model. The contours are shown on the *x*-*y* and *x*-*z* symmetry

planes of the nozzle/test box flowfield and on other planes of interest for the flowfield over the wedge model. Note that the wedge model was tested at 0.254 cm downstream of the nozzle exit with the leading edge of the wedge model on the nozzle centerline. The expansion waves emanating from the nozzle lip to the test box are seen in Fig. 6a. Downstream of the nozzle exit, these expansion waves and shear layer interact with the bow shock wave formed in front of the wedge model, which ordinarily affects the surface pressure and heat flux distributions of the wedge model. As expected, the effect of this interaction becomes significant when the model size and the nozzle exit diameter are comparable. Note that the nozzle exit diameter is only slightly larger than the width of the calibration wedge model.

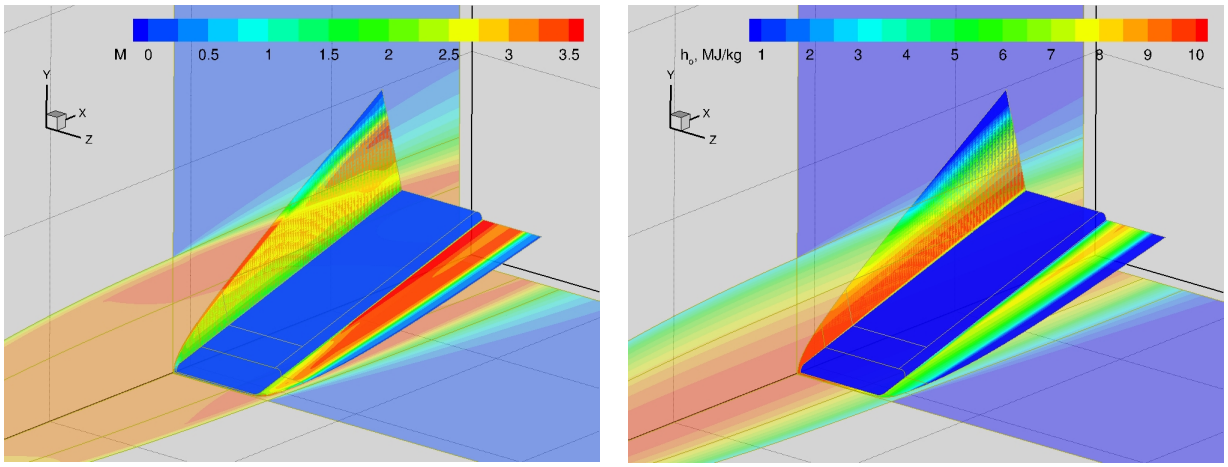

(a) Mach number **(b) total enthalpy**

Figure 6. Computed flowfield contours of the H3 Mach 3.3 nozzle and test box with the 15° calibration wedge model. $\dot{m}$ = 5.49 kg/s, h_{ob} = 7.1 MJ/kg, h_{ocl} = 9.9 MJ/kg, parabolic enthalpy profile, p_{box} = 760 torr, turbulent flow (SA model).

Figure 7 shows contours of the computed surface quantities (pressure, CWFC heat flux, and shear) of the 15° calibration wedge model and their centerline profiles at the condition shown in Fig. 6. The surface pressure decreases significantly along the wedge centerline, starting from the stagnation point as expected. The surface pressure of the test plate decreases gradually until about the s = 0.1 m location (Fig. 7a). This gradual decrease is mostly due to three-dimensional flow expansion over the side of the model. There is a significant pressure drop at about s = 0.105 m location and a subsequent increase at s = 0.14 m, both of which are the effects of expansion waves from the nozzle exit and their interactions with the bow shock wave of the wedge model. The s = 0.1 m station is the approximate location where the expansion waves start to interact, and the subsequent pressure increase is the result of wave reflection from the model surface. Since these expansion waves are three-dimensional, effects on the wedge surface pressure become larger at downstream locations and away from the wedge centerline (Fig. 7a). Similar to the surface pressure distribution, the surface heat flux and shear distributions (Fig. 7b and 7c) are affected accordingly, but the non-uniform total enthalpy distribution shown in Fig. 6b is also an important contributing factor.

Figure 8 shows computed calibration plate surface quantities and comparisons with the measured calibration plate data. The contour plots show computed surface pressure and heat flux on one half of the calibration plate. The symbols in the contour plots are the measurements at that location, color coded with the same contour levels. Note that both pressure and heat flux measurements for the three runs (total of five sweeps) were mostly consistent with each other. The computed and measured surface pressure values in Fig. 8a are in good agreement. Since there were only two pressure ports on the calibration plate (both upstream of the wave interaction region), the effects of wave interactions cannot be observed in the pressure measurements. It would be desirable to have pressure measurements at several locations along the plate centerline like the heat flux measurements. However, the heat flux measurements, especially those along the plate centerline in Fig. 8b, show some evidence of the wave interaction starting at a location between s = 0.07 m and 0.085 m. As discussed earlier, CFD simulations also predict this interaction as shown in Fig. 8b, but it is predicted to occur at a downstream location of s = 0.085-0.09 m. The source of this apparent discrepancy in the starting location of the wave interaction is not clear. There might possibly be two potential sources, both of which are related to the model location: the wedge model leading edge location with respect to the nozzle exit (x_{ml}), and the location of the wedge model with respect to the nozzle centerline at the time the heat flux measurements were reported.

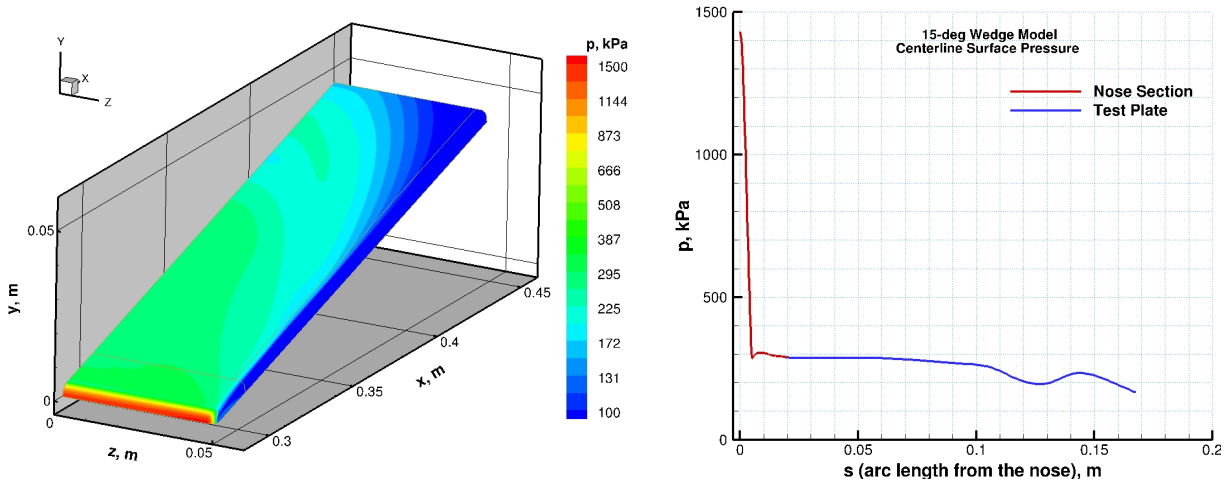

(a) pressure

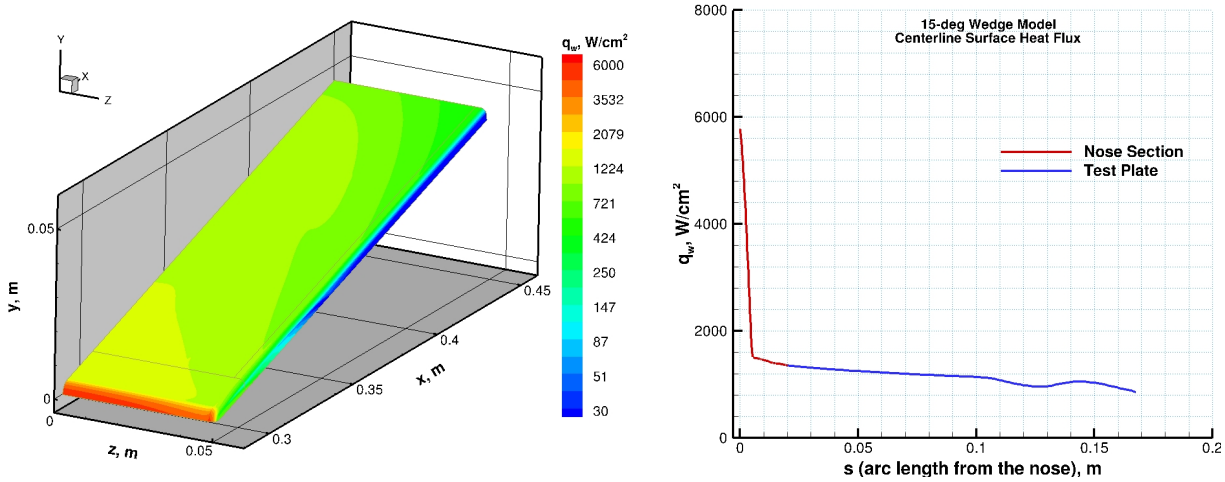

(b) CWFC heat flux

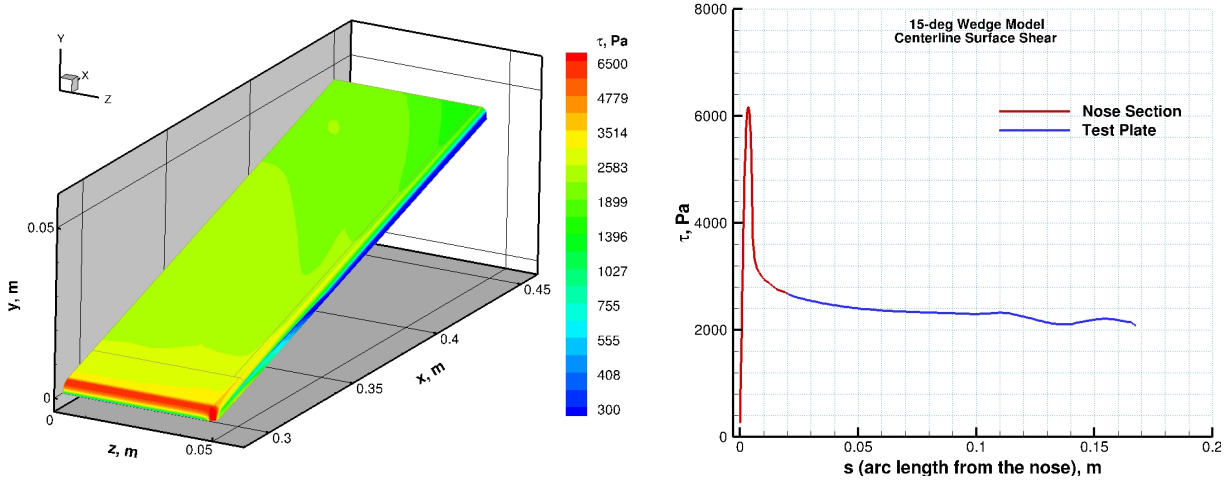

(c) shear

Figure 7. Computed surface contours and symmetry plane profiles of the 15° calibration wedge model. H3 Mach 3.3 nozzle flow: $\dot{m}$ = 5.49 kg/s, h_{ob} = 7.1 MJ/kg, h_{ocl} = 9.9 MJ/kg, parabolic enthalpy profile, p_{box} = 760 torr, turbulent flow (SA model).

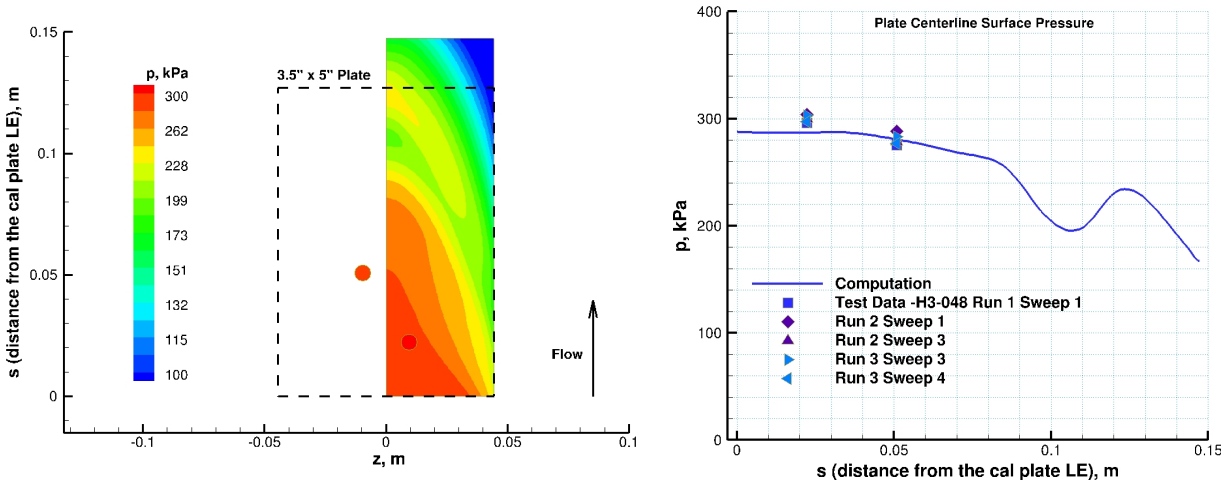

(a) pressure

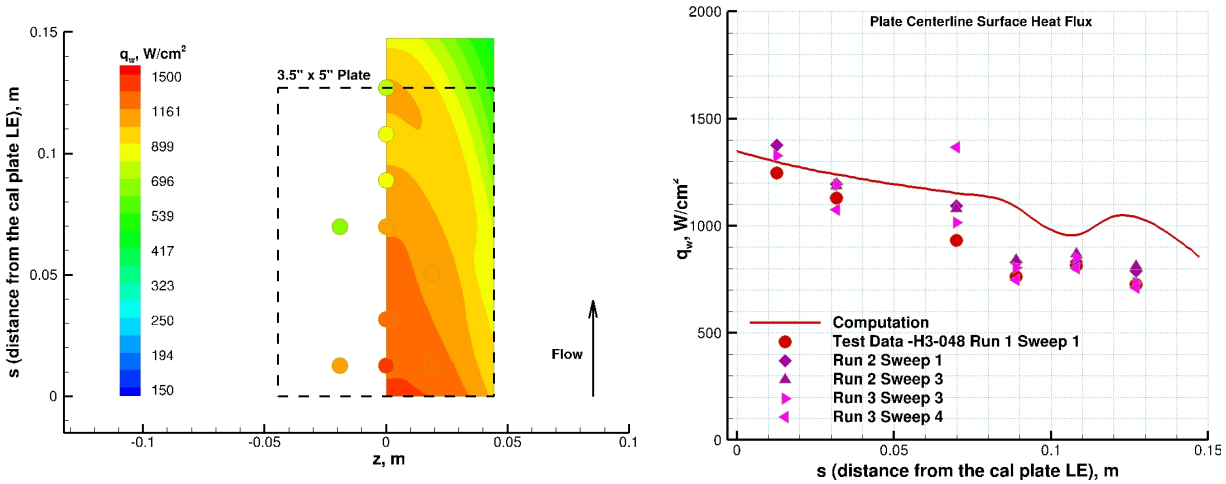

(b) CWFC heat flux

Figure 8. Computed surface quantities and comparisons with the 15° wedge calibration plate data. H3 Mach 3.3 nozzle flow: $\dot{m}$ = 5.49 kg/s, h_{ob} = 7.1 MJ/kg, h_{ocl} = 9.9 MJ/kg, parabolic enthalpy profile, p_{box} = 760 torr, turbulent flow (SA model). The contour plots include only Run 2 Sweep 1 data.

However, it would require moving the model leading edge at least 1 cm further downstream of the nozzle exit in CFD simulations to explain the earlier interaction (unlikely based on facility procedures). Overall, the computed heat flux values are considered in reasonably good agreement with the measurements, especially upstream of the wave interaction region. The heat flux measurements are estimated to be accurate to within ±15% and the pressure measurements to within ±5%.

A summary of CFD estimates for the 15° calibration wedge model is given in Table 2.

With a risk of digression here, sensitivity of the calibration wedge model CFD predictions to three turbulence models are presented from our earlier work [25]. The facility conditions are from H3-022 tests at arc heater pressure of 109 atm, mass flow rate of 5.67 kg/s, and estimated bulk enthalpy of 7.4 MJ/kg (similar to H3-048 tests but somewhat higher pressure and heating conditions). Figure 9 presents comparisons of computed surface pressure and heat flux along the calibration plate centerline for laminar and three turbulent models, and comparisons of the SA model results with the 2016 calibration plate pressure and heat flux data. The two-equation SST model simulations predict the transition just downstream of the calibration plate leading edge, and its predicted heat flux levels are generally higher than those of the one-equation SA model and the algebraic BL model simulations. Although the heat

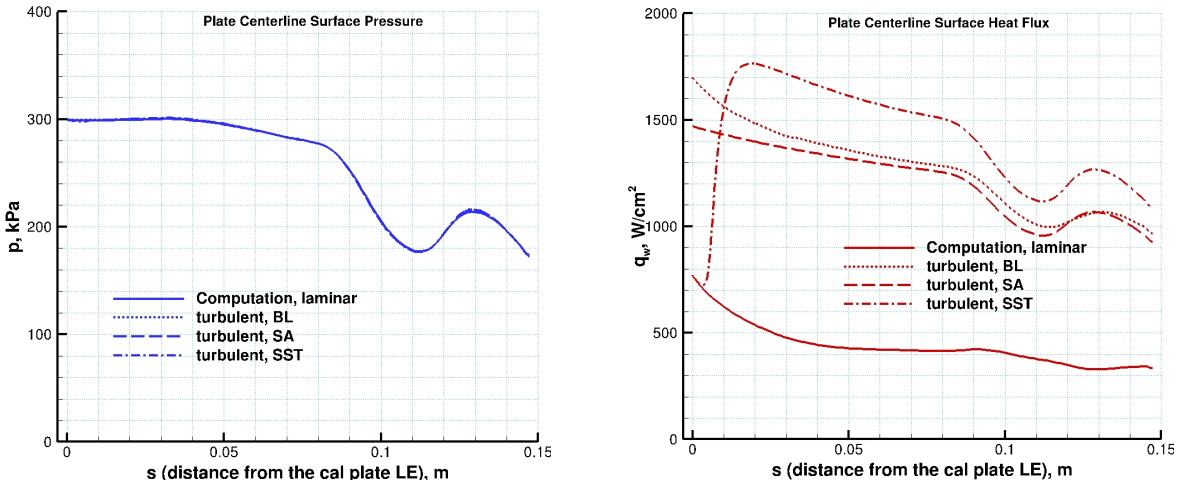

(a) comparisons of surface pressure and heat flux predictions, laminar and three turbulence models

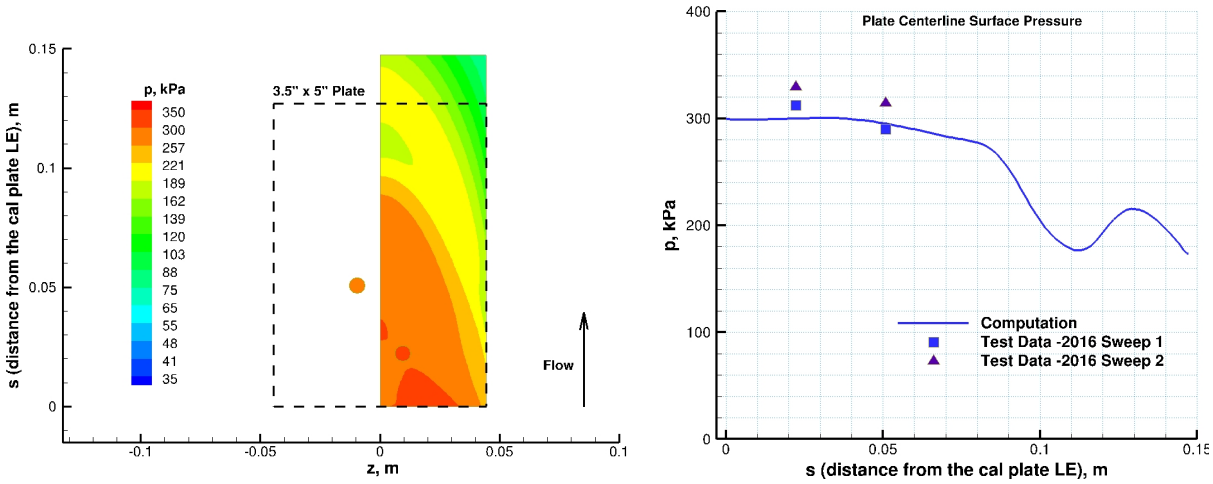

(b) comparisons of the SA results with the 2016 pressure data

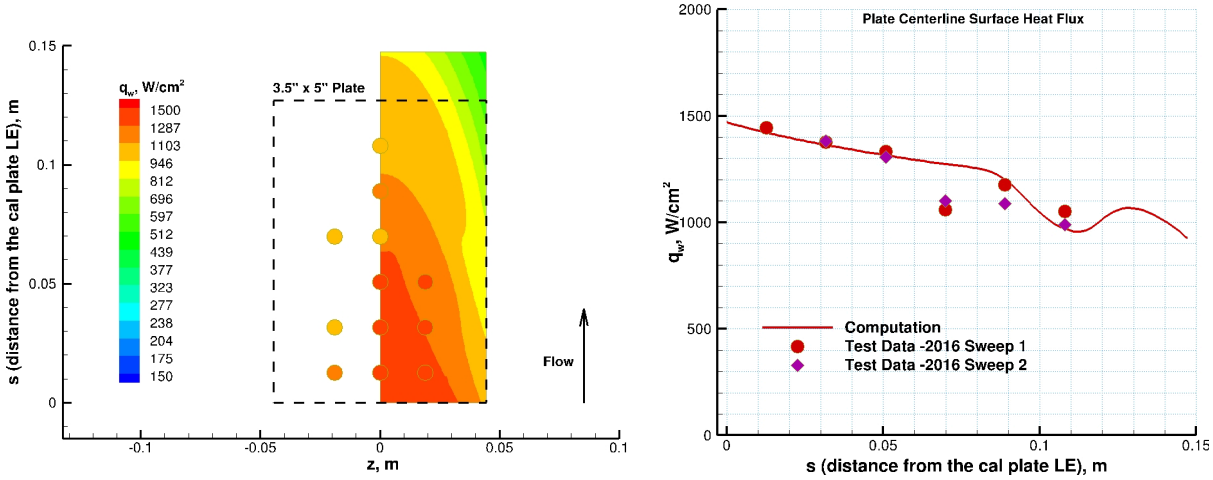

(c) comparisons of the SA results with the 2016 heat flux data (C_7 calorimeter was not working)

Figure 9. Comparisons of computed surface pressure and heat flux along the calibration plate centerline for laminar and three turbulent models, and comparisons of the SA model results with the 2016 15° wedge calibration plate data [24]: $\dot{m}$ = 5.67 kg/s, h_{ob} = 7.4 MJ/kg, h_{ocl} = 10.5 MJ/kg, parabolic enthalpy profile, turbulent flow. The contour plots include only Sweep 1 data.

flux results from the SA and BL turbulent models are in reasonably good agreement with each other along the plate centerline, the BL model results are unreliable in the wave interaction regions of the wedge flowfield. For the rest of the paper, only the SA model results are presented.

C. 15° one-sided standard TPS wedge model simulations

In this section, CFD simulation results for the one-sided standard TPS wedge model are presented. As mentioned earlier, the one-sided TPS wedge model geometry is different from the calibration wedge model (nose radius, width of the models, locations of the plate leading edge).

Figure 10 shows the computed pressure and total enthalpy contours of the H3 Mach 3.3 nozzle flow near the nozzle exit and test box with the 15° one-sided TPS wedge model. The contours are again shown on the symmetry planes of the nozzle/test box flowfield and on other planes of interest for the flowfield over the wedge model. The expansion waves from the nozzle lip and their interaction with the model shock wave downstream are clearly seen in the pressure contours, shown in Fig. 10a. Note that the width of the TPS wedge model is larger than the nozzle exit diameter. Because of this, in addition to the expansion wave interactions, the shear layer directly impinges on the model as seen from the contours on the *x*-*z* plane, which makes CFD simulations more challenging.

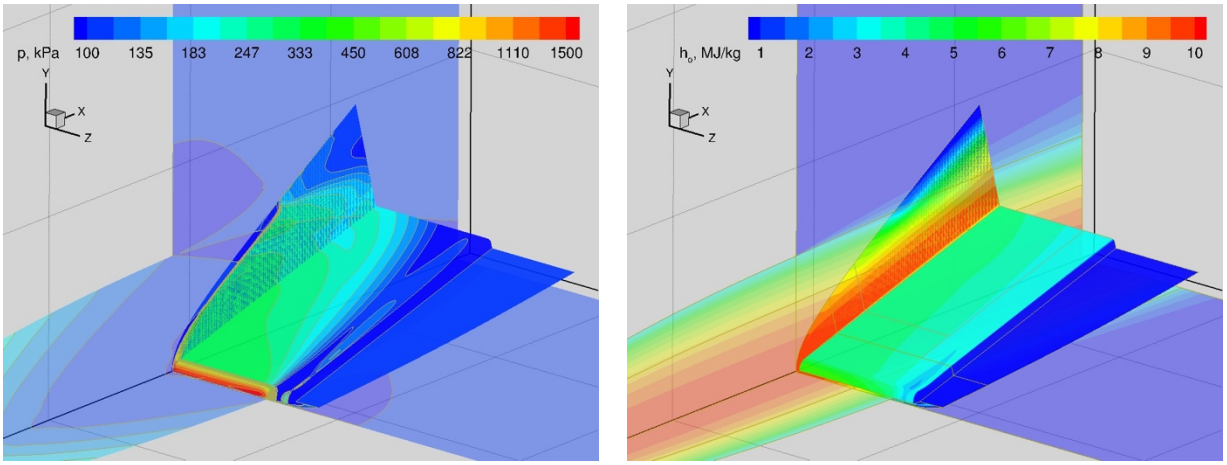

(a) pressure **(b) total enthalpy**

Figure 10. Computed flowfield contours of the H3 Mach 3.3 nozzle and test box with the 15° one-sided TPS wedge model. $\dot{m}$ = 5.49 kg/s, h_{ob} = 7.1 MJ/kg, h_{ocl} = 9.9 MJ/kg, parabolic enthalpy profile, p_{box} = 760 torr, turbulent flow (SA model).

Figure 11 shows contours of the computed surface quantities (pressure, HWFC heat flux, and shear) of the 15° TPS wedge model and their centerline profiles. Note that the surface heat flux and temperatures for this case are computed using radiative equilibrium boundary condition since the TPS wedge model is not water-cooled. The hot-wall fully-catalytic (HWFC) heat flux predictions are also important for flight to arc-jet test traceability purposes since the flight environment definition is usually based on these quantities. Although the line plots of surface pressure and heat flux and shear along the plate centerline in Fig. 11 show distributions similar to those in Fig. 7, additional shear layer impingement effects are seen in the surface contour plots. Since the wedge model is wider than the nozzle exit diameter, significant spanwise gradients are predicted in surface pressure and heat flux of the test articles. The presented surface quantities are used as inputs for the TPS material response analysis of the test articles [8].

A summary of CFD estimates for the 15° one-sided standard TPS wedge model is given in Table 2. It should be mentioned that the HWFC and surface shear values presented here correspond to smooth surfaces (no heating or shear augmentations are included for the TPS surface roughness developed in testing).

D. 15° one-sided shoulder feature wedge model simulations

In this section, CFD simulation results for the 15° one-sided shoulder feature wedge model are presented.

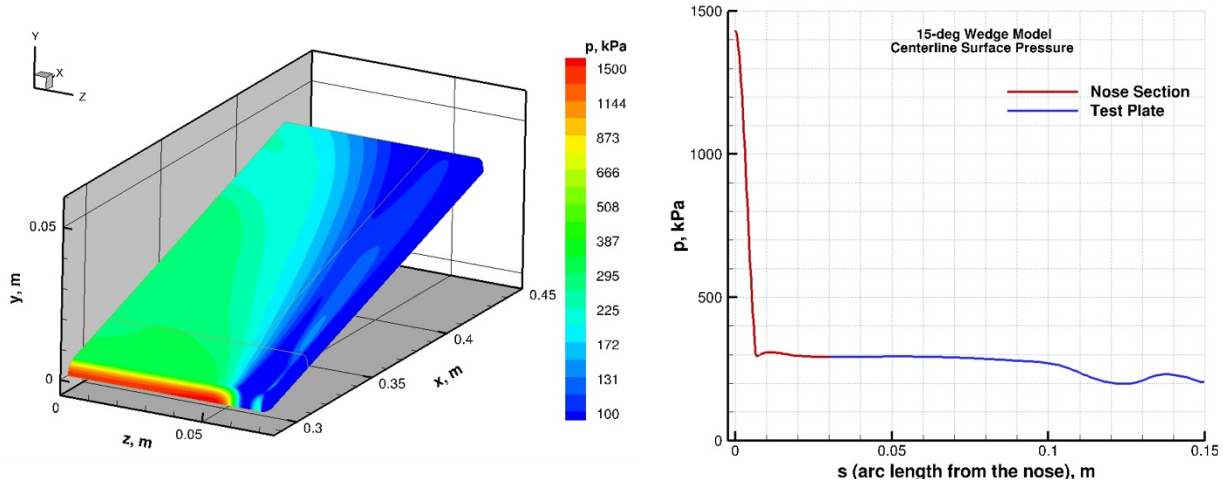

(a) pressure

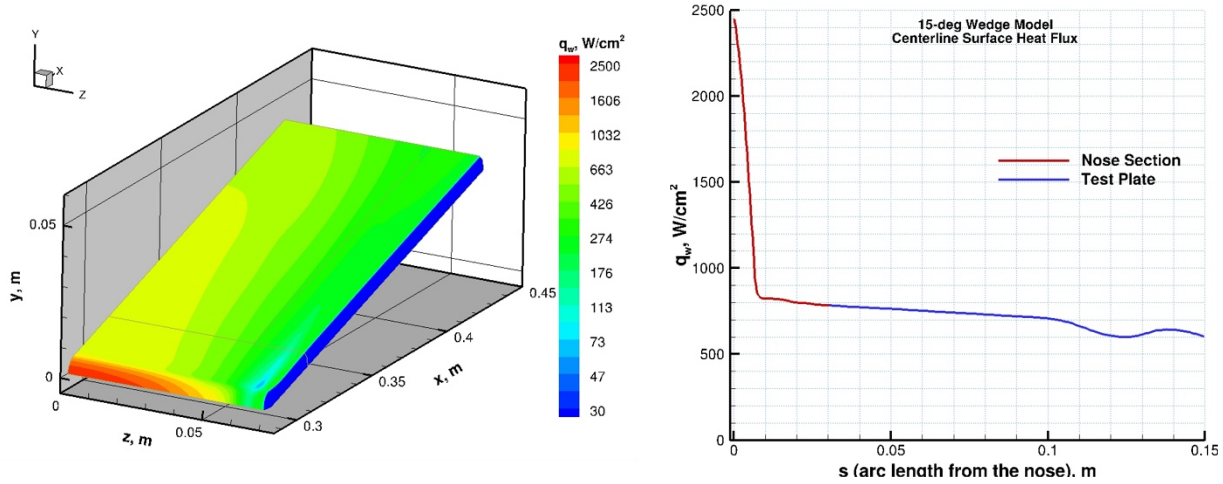

(b) HWFC heat flux

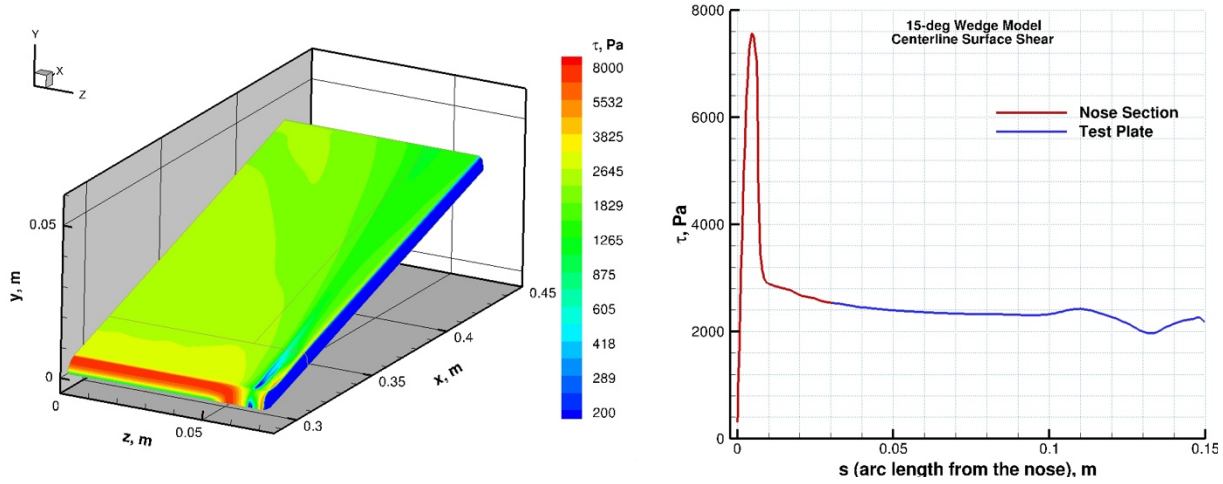

(c) shear

Figure 11. Computed surface contours and symmetry plane profiles of the 15° one-sided TPS wedge model. H3 Mach 3.3 nozzle flow: $\dot{m}$ = 5.49 kg/s, h_{ob} = 7.1 MJ/kg, h_{ocl} = 9.9 MJ/kg, parabolic enthalpy profile, p_{box} = 760 torr, turbulent flow (SA model).

Figure 12 shows the computed pressure and total enthalpy contours of the H3 Mach 3.3 nozzle flow near the nozzle exit and test box with the 15° one-sided shoulder feature wedge model. The contours are again shown on the symmetry planes of the nozzle/test box flowfield and on other planes of interest for the flowfield over the wedge model. The expansion waves from the nozzle lip and their interaction with the model shock wave downstream are seen in the pressure contours shown in Fig. 12a. However, their interaction occurs downstream of the wedge shoulder region and does not influence surface quantities of the test plate. Since this wedge model was intended to test a shoulder feature like the MSR-EES TPS shoulder geometry, it was intentionally designed as a shorter or truncated version of the standard TPS wedge model based on pretest CFD simulations so that evaluation of the shoulder TPS performance would not be affected by the expansion wave interactions and their larger uncertainties. Again, the width of the feature wedge model is larger than the nozzle exit diameter, so the shear layer impingement on the model is still present as seen in the *x-z* plane contours.

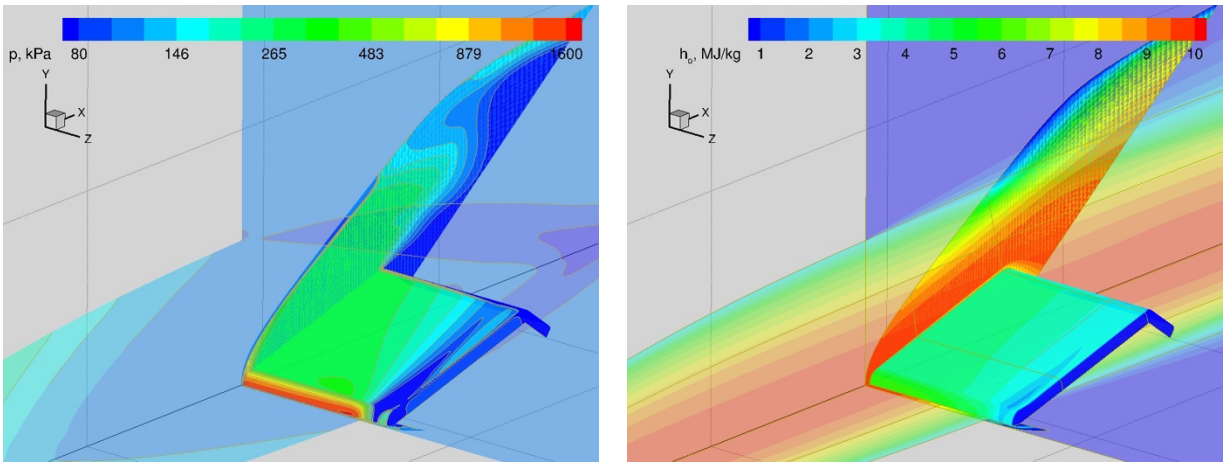

(a) pressure **(b) total enthalpy**

Figure 12. Computed flowfield contours of the H3 Mach 3.3 nozzle and test box with the 15° one-sided shoulder feature wedge model. $\dot{m}$ = 5.49 kg/s, h_{ob} = 7.1 MJ/kg, h_{ocl} = 9.9 MJ/kg, parabolic enthalpy profile, p_{box} = 760 torr, turbulent flow (SA model).

Figure 13 shows contours of the computed surface quantities (pressure, HWFC heat flux, and shear) of the 15° shoulder feature wedge model and their centerline profiles. Note that the surface pressure and heat flux along the plate centerline are relatively uniform all the way up to the plate shoulder. Clearly, the expansion wave interaction effects are not felt by the shoulder region of the test article. Since testing TPS performance near the shoulder region is the primary objective for this model, predicted surface quantities near the shoulder and on the back plate are of interest. As the flow expands around the shoulder region, both surface pressure and heat flux levels drop precipitously, while the shear levels increase first, reaching the maximum value over 4300 Pa, and then drop too. The CFD simulations predict that the flow remains attached near the *x-y* symmetry plane, but it is separated on the back side of the shoulder region away from the centerline, as can be observed from the reductions in the heat flux and shear contours in Figs. 13b and 13c.

Figure 14 shows the distributions of the predicted boundary layer thickness and edge Mach number along the shoulder feature wedge model centerline and boundary layer profiles at two test plate locations. The boundary layer thickness, edge Mach number and other edge flow properties are often important to evaluate the performance of TPS materials and to make comparisons with the corresponding flight environments. For this case, the boundary layer thickness on the test plate increases gradually from its leading edge to the shoulder region while the edge Mach number remains relatively constant. As the flow turns the corner at the shoulder, both δ and M_e increase dramatically. N_2, O, O_2, and NO are the primary species at the boundary layer edge. The flow composition and edge flow conditions do not change significantly from the plate leading edge to the shoulder, only the growth in boundary layer thickness.

A summary of CFD estimates for the 15° one-sided shoulder feature wedge model is given in Table 2.

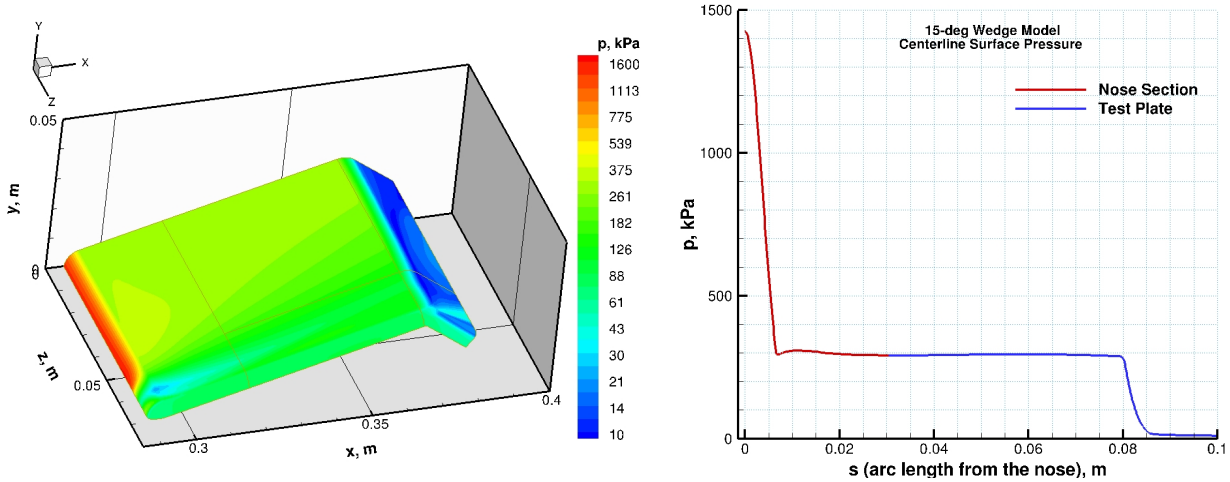

(a) pressure

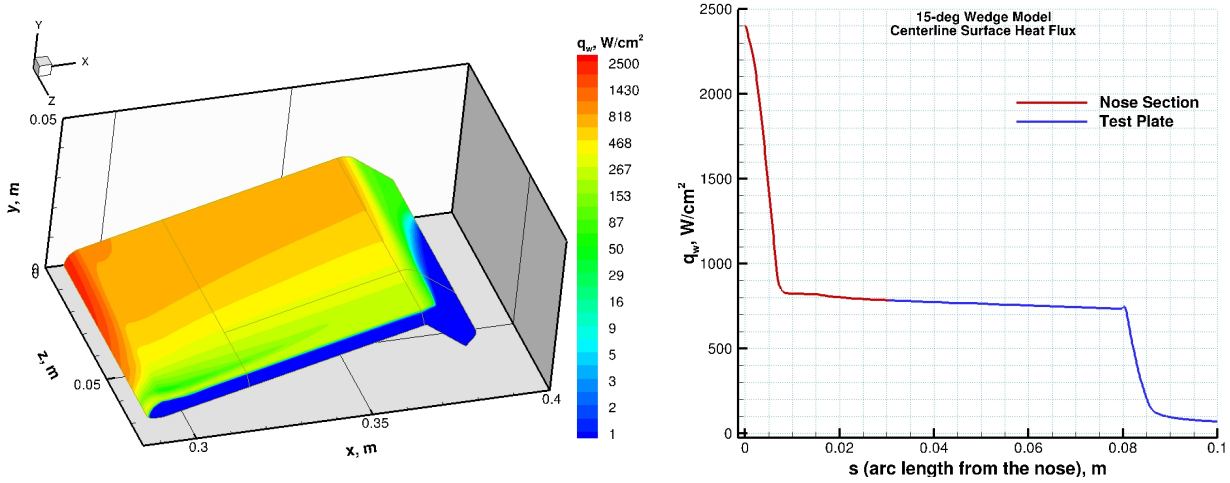

(b) HWFC heat flux

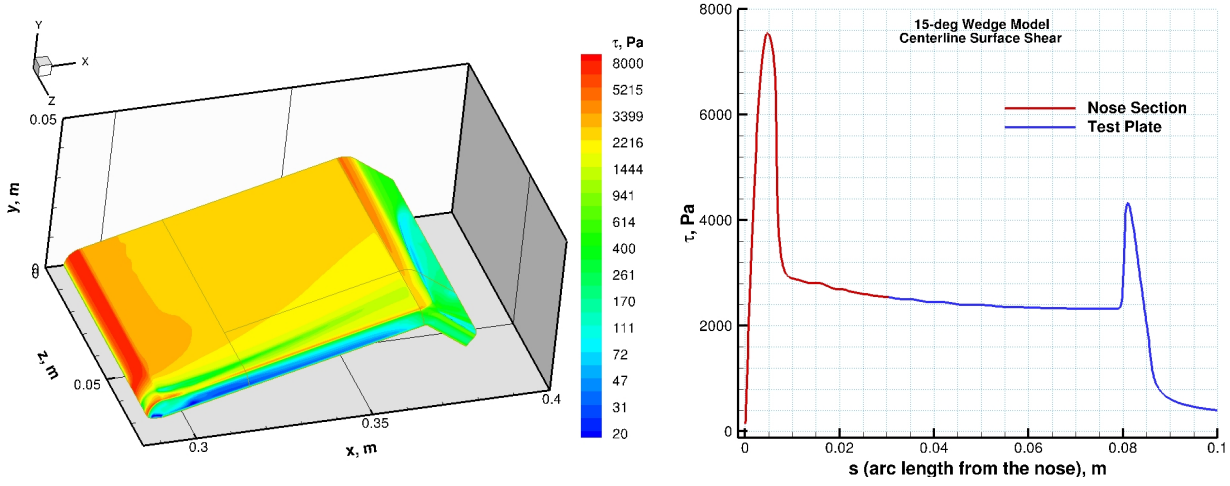

(c) shear

Figure 13. Computed surface contours and symmetry plane profiles of the 15° one-sided shoulder feature wedge model. H3 Mach 3.3 nozzle flow: $\dot{m}$ = 5.49 kg/s, h_{ob} = 7.1 MJ/kg, h_{ocl} = 9.9 MJ/kg, parabolic enthalpy profile, p_{box} = 760 torr, turbulent flow (SA model).

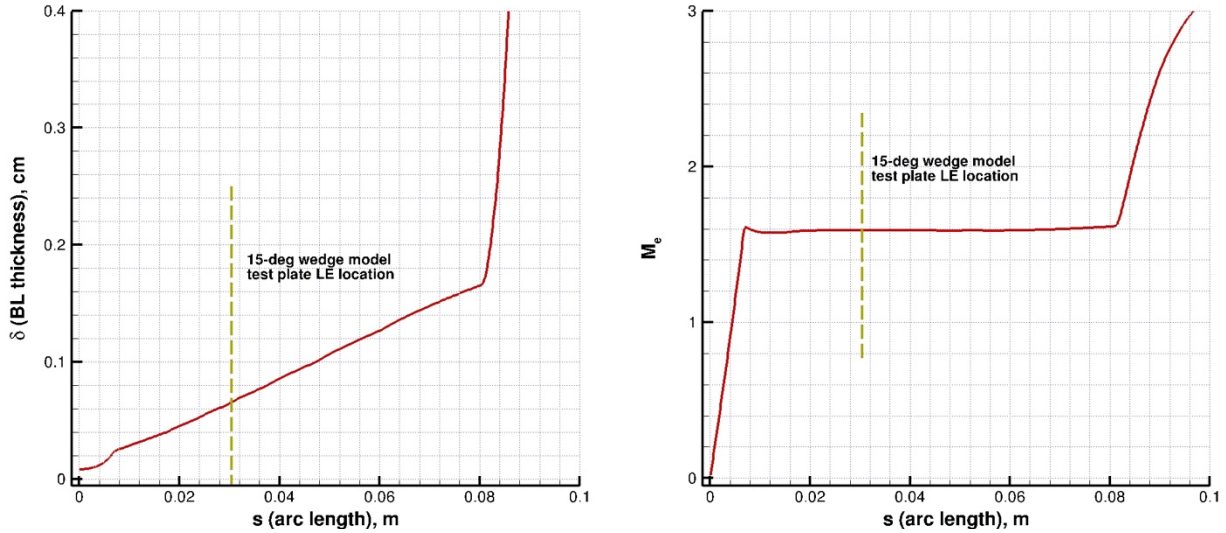

(a) boundary layer thickness and edge Mach number

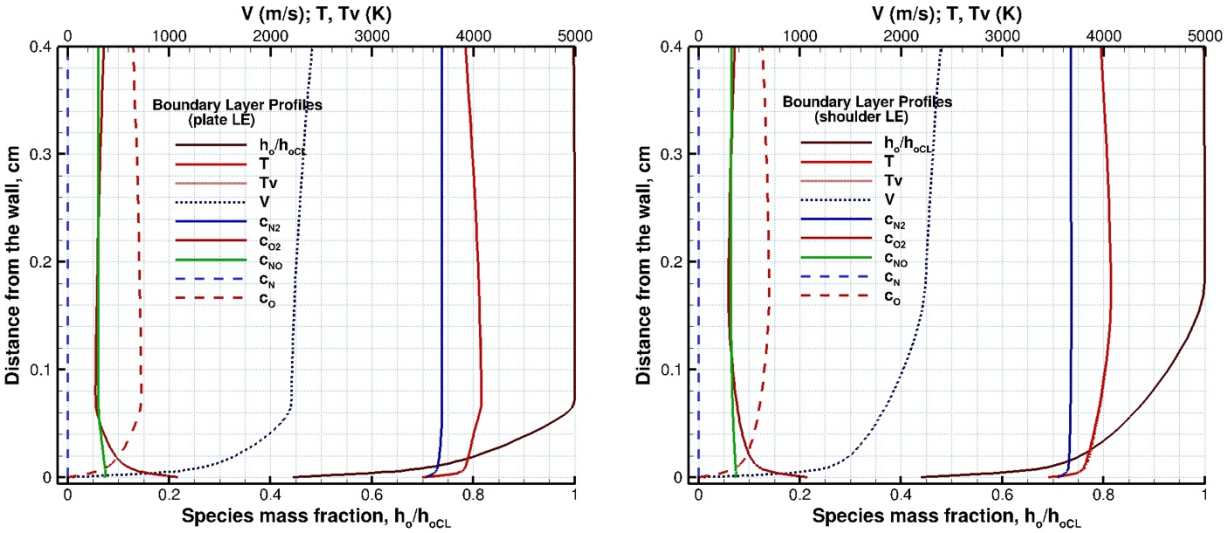

(b) boundary layer profiles

Figure 14. Computed boundary layer thickness and edge Mach number along the 15° shoulder feature wedge model centerline and boundary layer profiles at two test plate locations.

E. Recessed model simulations: the shoulder feature wedge model

One of the complicating factors in analysis of the test data in the wedge configuration is that test article ablation and its subsequent shape change during the test affect the test article surface conditions and make interpretation of the test data difficult. Since TPS material response analyses typically use the CFD predictions for the initial shape, it is important to assess the extent of the shape change and how it would affect the surface quantities.

Figure 15 shows an example of a recessed shoulder feature wedge model with the measured recession map of the test plate based on pretest and post-test laser scans (74-04 model). Based on Fig. 15 and other post-test articles not shown here but presented in [8], the following observations are made: (1) there is noticeable recession at the nose section of the wedge model but the recession just upstream of the test plate is negligible; (2) due to the test plate recession, a cavity or a concave surface is formed on the test plate, with the maximum recession occurring along the centerline and almost no recession on the side of the test plate; (3) the downstream shoulder is sharpened or gets a reduced corner radius; (4) a relatively rough surface has developed as the test article recessed during the test.

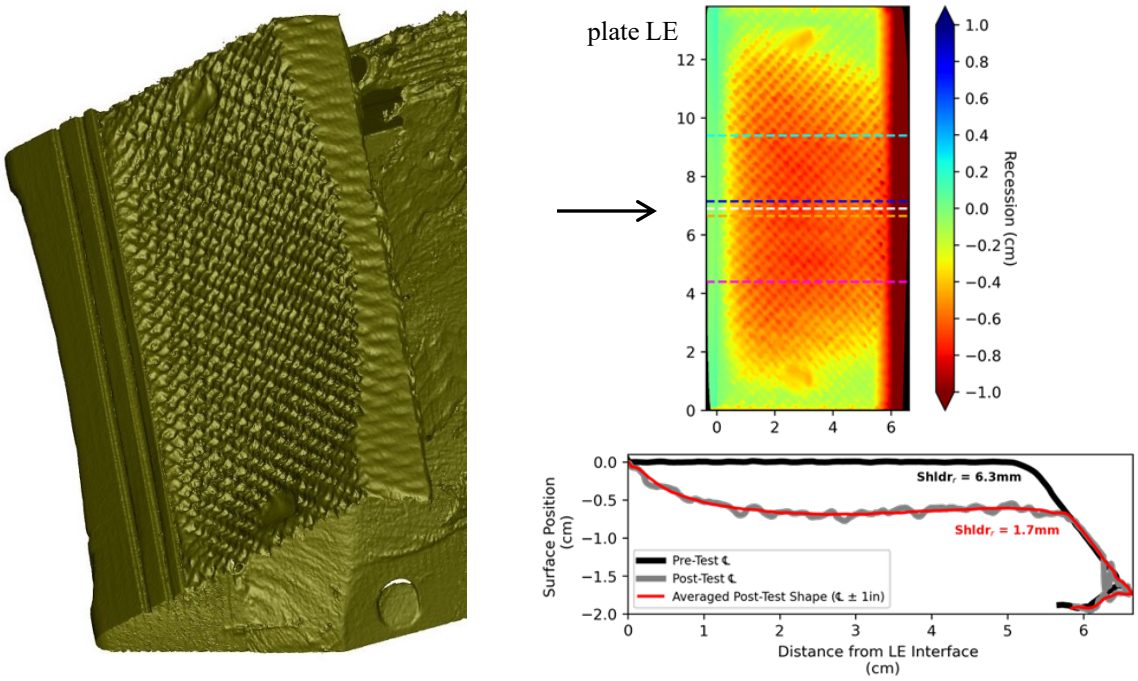

(a) a post-test laser scan image of the 74-04 model **(b) measured recession map and centerline profile**

Figure 15. An example of a recessed shoulder feature wedge model with the measured recession map of the test plate based on pretest and post-test laser scans.

In order to assess effects of the shape change on test plate surface quantities, CFD simulations are performed for one of the tested shoulder feature wedge models (74-04 model). These simulations use an idealized recessed model geometry: it is an approximate model with smooth surfaces, but it includes some of the quantitative and qualitative features observed in the post-test article (recession of the nose section, a cavity formation on the test plate, the maximum recession and its location along the plate centerline, and the sharpening of the downstream shoulder radius). These simulations are intended to assess the change in heating environments during the test as well as provide insights into the developed flowfield features resulting from the test article recession.

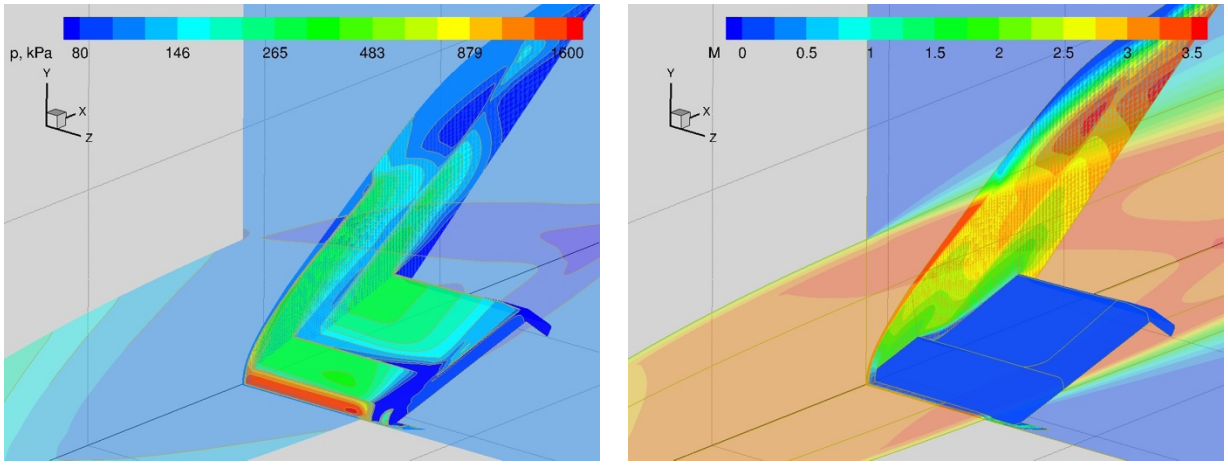

(a) pressure **(b) Mach number**

Figure 16. Computed flowfield contours of the H3 Mach 3.3 nozzle and test box with the idealized recessed feature wedge model. $\dot{m}$ = 5.49 kg/s, h_{ob} = 7.1 MJ/kg, h_{ocl} = 9.9 MJ/kg, parabolic enthalpy profile, p_{box} = 760 torr, turbulent flow (SA model).

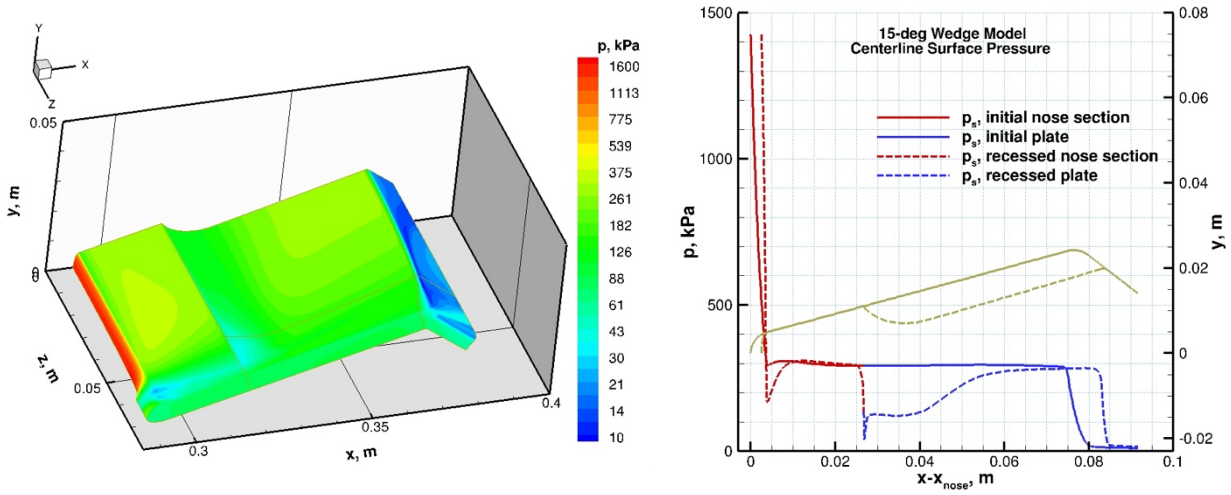

(a) pressure

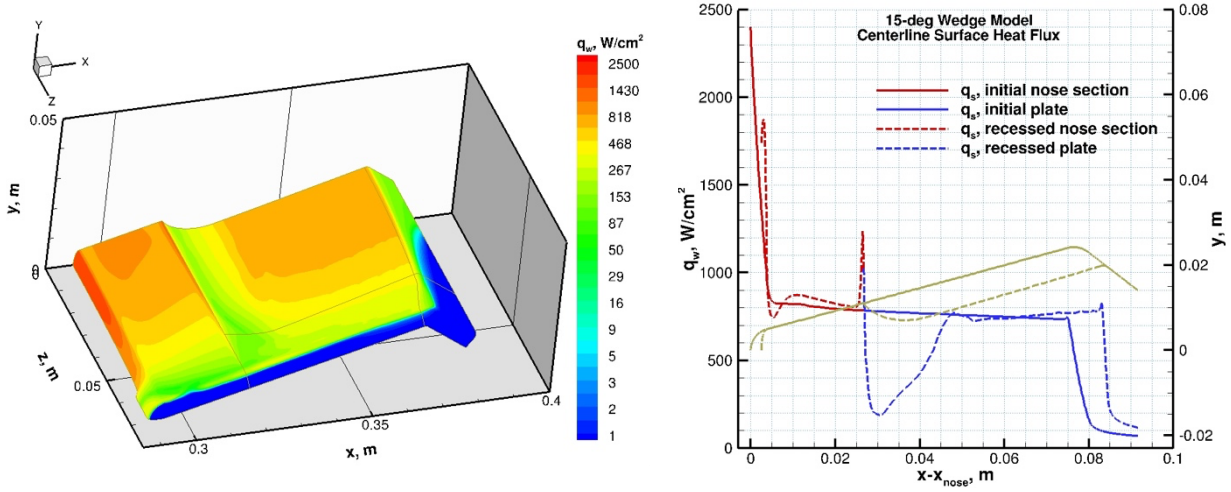

(b) HWFC heat flux

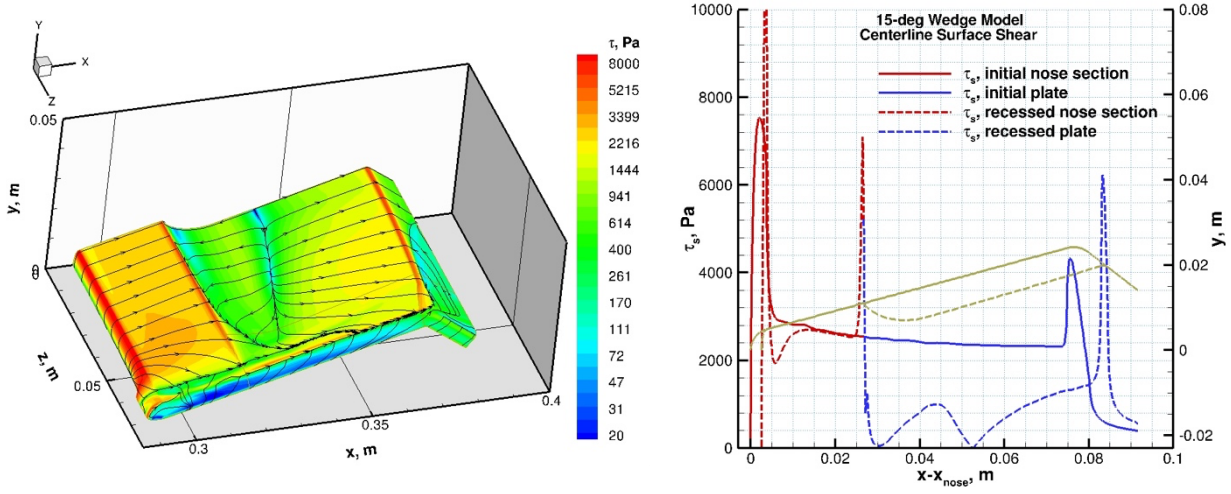

(c) shear with surface streamlines

Figure 17. Computed surface contours and symmetry plane profiles of the idealized recessed feature wedge model. H3 Mach 3.3 nozzle flow: $\dot{m}$ = 5.49 kg/s, h_{ob} = 7.1 MJ/kg, h_{ocl} = 9.9 MJ/kg, parabolic enthalpy profile, p_{box} = 760 torr, turbulent flow (SA model).

Figure 16 shows the computed pressure and Mach number contours of the H3 Mach 3.3 nozzle flow near the nozzle exit and test box with the idealized recessed feature wedge model. The contours are shown on the symmetry planes and on other planes of interest for the flowfield over the wedge model as before. As seen in the *x*-*y* symmetry plane pressure and Mach number contours, starting from the plate leading edge, the flow goes through rapid expansion which results in flow separation. The flow reattaches downstream, forming an oblique shock wave (the reattachment shock), and then it goes through another rapid expansion at the recessed shoulder.

Figure 17 shows contours of the computed surface quantities (pressure, HWFC heat flux, and shear) of the recessed shoulder feature wedge model and their centerline profiles. The pale green lines in the line plots represent initial and recessed surface profiles on the centerline. Note that that surface pressure and heat flux are reduced significantly near the plate leading edge due to formation of a cavity resulting in flow separation. When the flow reattaches downstream, surface pressure and heat flux values approach to their initial levels while the surface shear remains at significantly lower levels. However, the peak shoulder shear value for the recessed model is increased, mostly due to sharpening of the shoulder (the recessed radius of 1.7 mm vs the initial radius of 6 mm) as has been observed in the tests. Note that the movement of the shoulder downstream makes it impossible to predict the surface recession near the shoulder using the CFD predictions for the initial shape and one-dimensional material response analysis. In Fig. 17c, surface shear contours are shown with surface streamlines, which are informative to map out important flow features. As expected, stagnant and separated regions in the flowfield are the regions with relatively low shear levels. Two separated regions, one just downstream of the plate leading edge, and another one on the back side of the shoulder, are clearly seen. Also, these streamlines show the flow reattachment line after the recirculation region on the test plate, which is manifested by increased shear values downstream.

F. Simulations of two circular cavities: shallow and deep cavities

In this section, CFD simulation results for the 15° one-sided standard TPS wedge model with two circular cavities are presented.

As mentioned earlier, some of the standard TPS wedge test articles included two circular cavities (Fig. 1f). These cavities were intended to simulate potential TPS damage. These two cavities are referred to here as the shallow and deep cavities: each had a diameter of 1.524 cm (0.6 in), and the center of each cavity was located 2.54 cm away from the wedge plate symmetry plane. The depth of the shallow cavity was 0.127 cm (the streamwise cavity length to the depth ratio or D/H of 12), while the depth of the deep cavity was 0.635 cm (or D/H ratio of 2.4). The two cavity depths were chosen to represent two limiting cases of idealized closed and open cavities (e.g., see Everhart [26], Everhart and Greene [27], and the references therein). There are several factors that determine the extent of flow penetration and heating distributions in a cavity flow (laminar, turbulent, boundary layer thickness and edge Mach number, pressure gradient, etc.), and the most important geometric factor for idealized cavities is the streamwise cavity length to depth ratio. Even though the flow inside cavities is complex and three-dimensional, the flow typically goes through an expansion at the cavity leading edge followed by a compression at the cavity floor, which is followed by flow impingement and expansion on the downstream trailing edges of the cavity. The difference between these two cavity flows is that the shallow cavity can possibly be characterized as a “closed” cavity while the deep cavity is likely an “open” cavity. In a “closed” cavity (the shallow cavity), the incoming flow is able to turn into the cavity and attach to the floor before exiting the cavity, while in an “open” cavity (the deep cavity), the incoming flow separates. It does not attach to the cavity floor, but it impinges on the downstream wall [26].

To provide further insight into the predicted flow structures within these two cavities, computed flowfield pressure contours with streamlines on the *x*-*y* plane of interest at $z = 2.54$ cm are presented in Fig. 18. The *x*-*y* plane at $z = 2.54$ cm goes through the center of each cavity considered, and it approximately represents the streamwise cavity symmetry plane. Note that the computed streamlines for the shallow cavity in Fig. 18a show all the characteristics of a closed cavity (e.g., flow attachment on the floor), while the corresponding streamlines for the deep cavity in Fig. 18b have the characteristics of an open cavity. It should be mentioned that for CFD simulations of the wedge model with the two circular cavities, two separate simulations were performed, one for each cavity on one half of the plate, and the cavity center being on the *x*-*y* plane at $z = 2.54$ cm for both.

However, it should be noted that the present cavity flowfields have significant differences from the idealized shallow and deep cavities described above. Since the center of each circular cavity is not on the plate symmetry plane, the flow approaching cavities is not symmetric and is highly non-uniform with respect to the streamwise cavity

symmetry plane. There are also significant pressure gradients on the plate at locations of these cavities. Any pressure gradient of the on-coming flow over the cavity is expected to influence the extent of the flow penetration into the cavity. For instance, Fig. 19 shows the computed surface pressure and heat flux contours over the plate with the shallow cavity. The surface pressure and heat flux distributions upstream of the cavity are highly non-uniform, as also would be expected from the smooth surface simulations presented in Section C. Clearly, the presence of the cavity on the plate surface disturbs the flow, thus affecting distributions of all surface quantities downstream (e.g., see corresponding contour plots in Fig. 11 for comparison with Fig. 19).

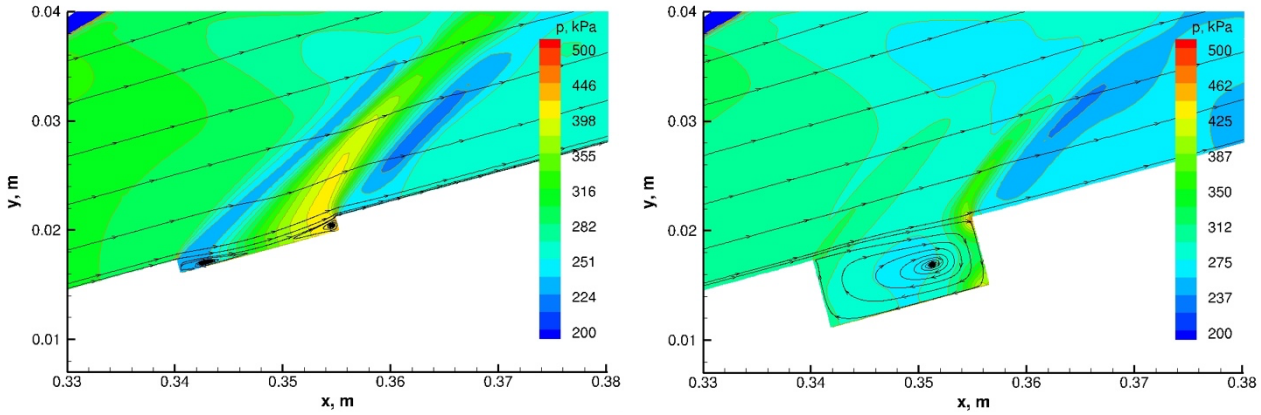

(a) shallow cavity **(b) deep cavity**

Figure 18. Computed pressure contours and streamlines on the *x*-*y* plane at $z = 2.54$ cm for the two circular cavities. H3 Mach 3.3 nozzle flow: $\dot{m}$ = 5.49 kg/s, h_{ob} = 7.1 MJ/kg, h_{ocl} = 9.9 MJ/kg, parabolic enthalpy profile, p_{box} = 760 torr, turbulent flow (SA model).

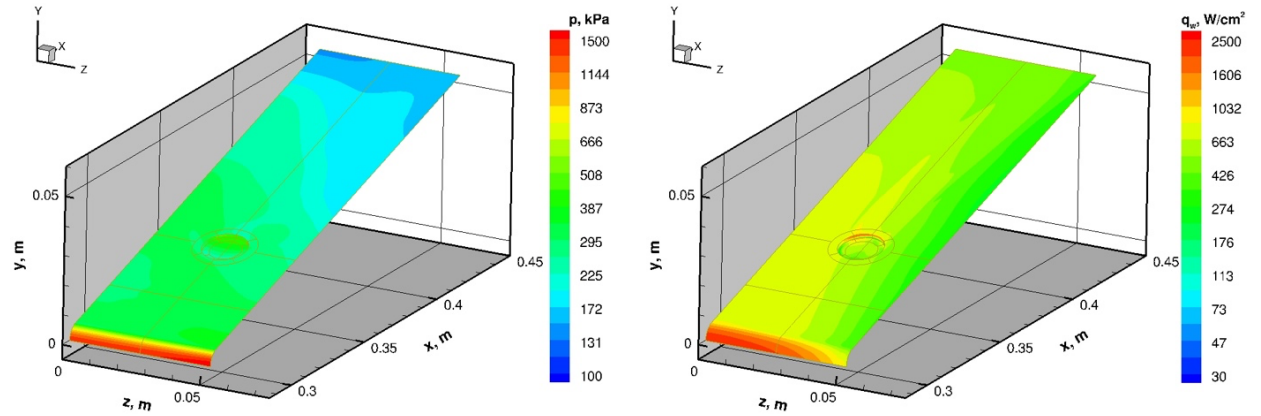

(a) pressure **(b) heat flux**

Figure 19. Computed surface contours of the 15° one-sided TPS wedge model with the shallow cavity. H3 Mach 3.3 nozzle flow: $\dot{m}$ = 5.49 kg/s, h_{ob} = 7.1 MJ/kg, h_{ocl} = 9.9 MJ/kg, parabolic enthalpy profile, p_{box} = 760 torr, turbulent flow (SA model).

Figures 20 and 21 present computed contours of surface pressure, heat flux and shear and their corresponding *x*-*y* plane profiles at $z = 2.54$ cm near the shallow and deep cavity, respectively. Again, to make interpretation of the surface line plots easier, the cavity geometries are also shown.

For the shallow cavity results in Fig. 20, as expected, the flow goes through an expansion at the cavity leading edge followed by a compression and reattachment on the cavity floor, which is followed by a flow impingement and expansion on the downstream trailing edge of the cavity. Complex and three-dimensional flow features and non-uniform upstream effects are all evident in these contour plots. Note that the left side of the cavity closer to the plate centerline show higher pressure, heat flux and shear levels due to the non-uniform upstream conditions. Also note that there are two distinct augmented heating regions predicted on the cavity floor near the cavity trailing edge (Fig. 20b),

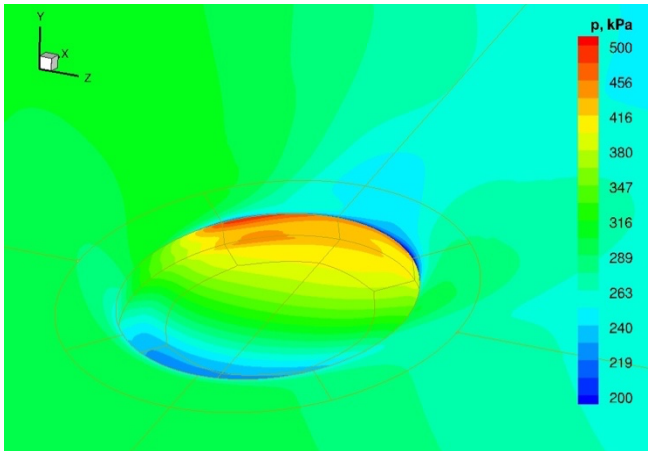

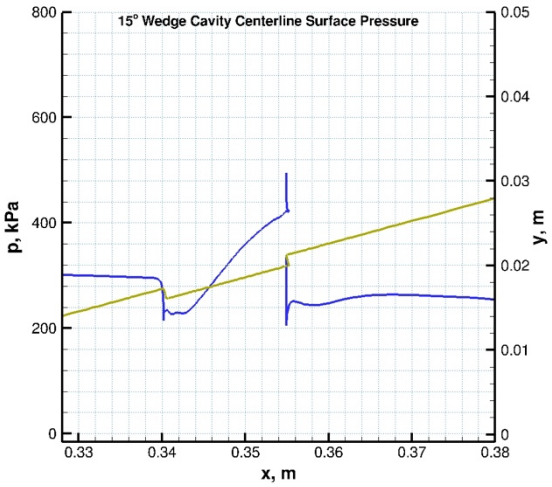

(a) pressure

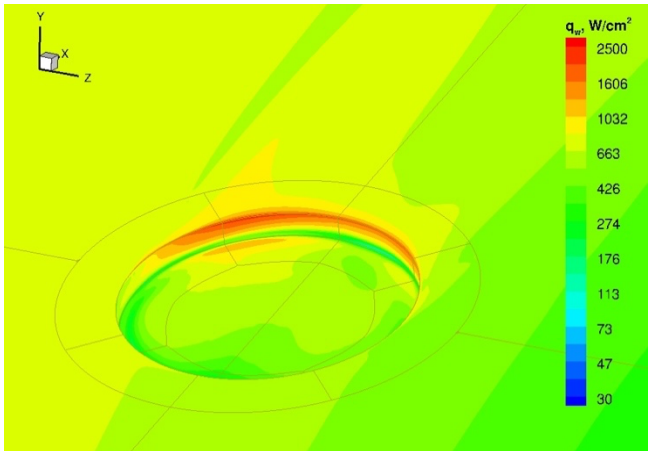

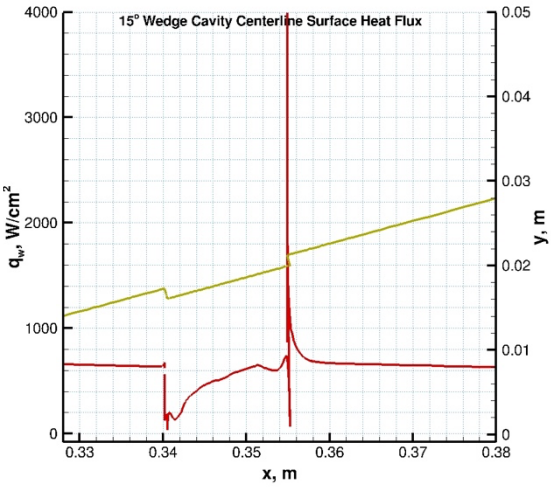

(b) HWFC heat flux

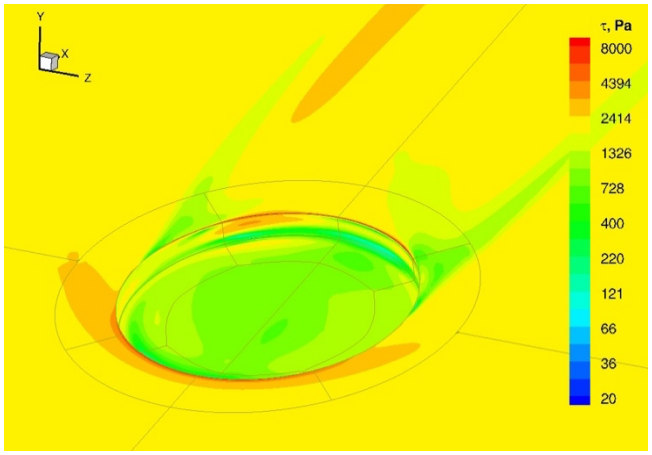

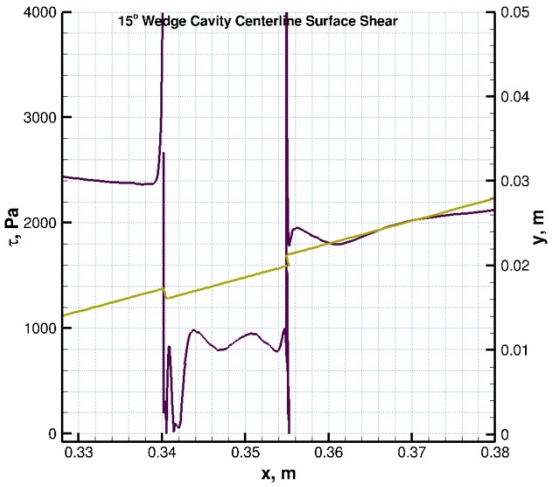

(c) shear

Figure 20. Computed surface contours and their corresponding *x*-*y* plane profiles at $z = 2.54$ cm near the shallow cavity. H3 Mach 3.3 nozzle flow: $\dot{m} = 5.49$ kg/s, $h_{ob} = 7.1$ MJ/kg, $h_{ocl} = 9.9$ MJ/kg, parabolic enthalpy profile, $p_{box} = 760$ torr, turbulent flow (SA model).

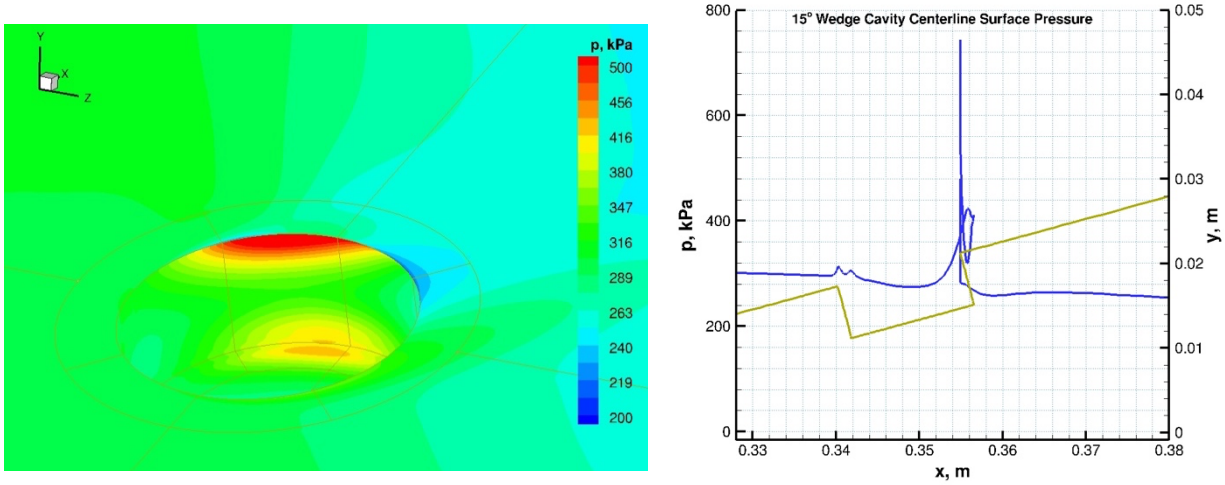

(a) pressure

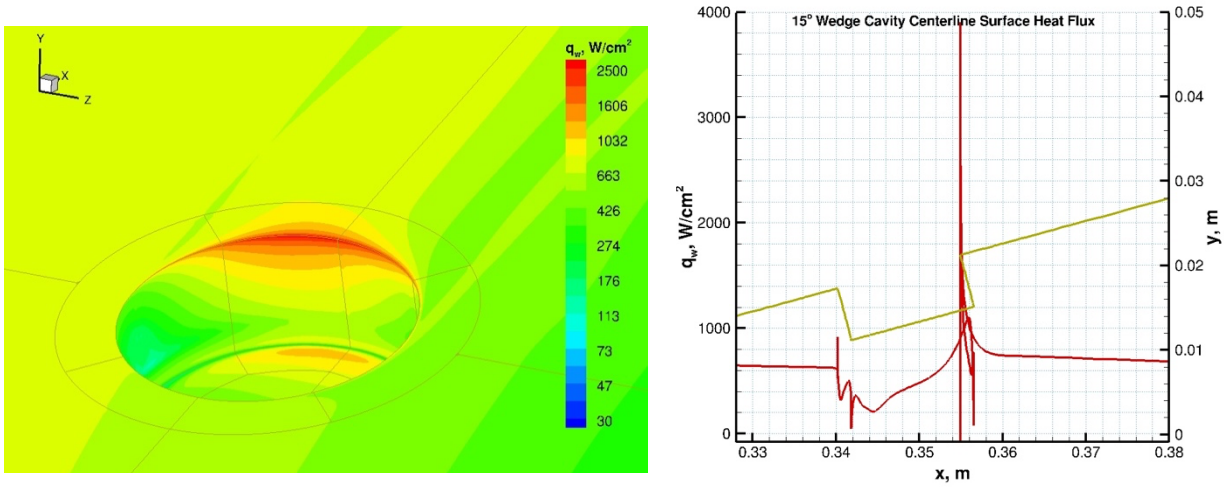

(b) HWFC heat flux

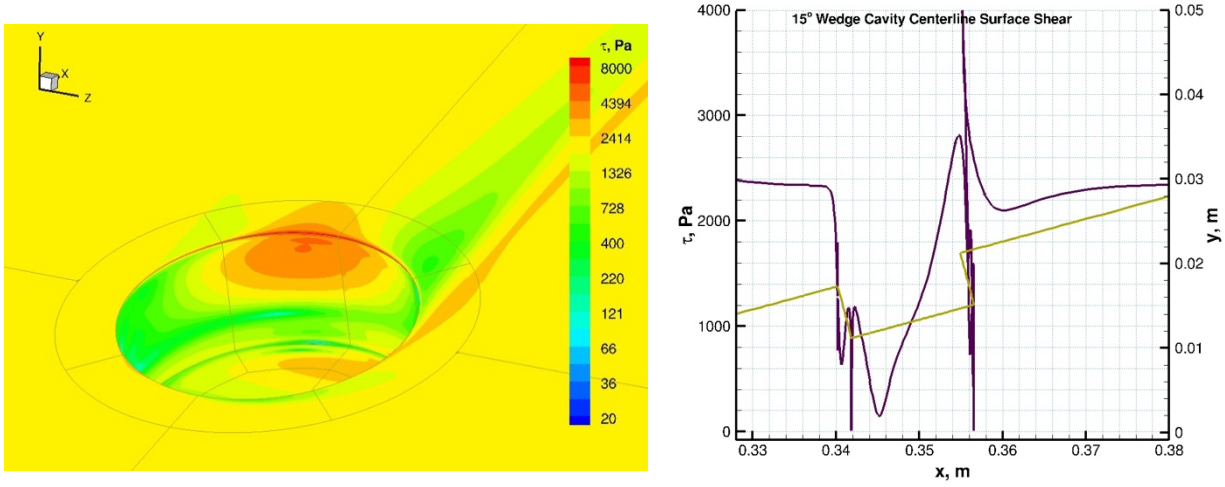

(c) shear

Figure 21. Computed surface contours and their corresponding *x*-*y* plane profiles at z=2.54 cm near the deep cavity. H3 Mach 3.3 nozzle flow: $\dot{m}$ = 5.49 kg/s, h_{ob} = 7.1 MJ/kg, h_{ocl} = 9.9 MJ/kg, parabolic enthalpy profile, p_{box} = 760 torr, turbulent flow (SA model).

the left side having higher heating levels. The elevated pressure, heat flux and shear levels at the cavity floor are indicative of an attached flow. Note that the elevated shear levels just upstream of the cavity leading edge are also indicative of the closed cavity, as they result from the acceleration of the flow turning into the cavity as shown Fig. 18a.

For the deep cavity results in Fig. 21, predicted surface contours and line plots are markedly different from those shown in Fig. 20. As seen in Fig. 21a, the pressure levels in the cavity remain relatively unchanged, except near the cavity trailing edge. The predicted heating and shear levels on the cavity floor in Figs. 21b and 21c are lower than those just upstream of the cavity. In contrast to the shallow cavity results in Figs. 20b and 20c, there are several differences. There is only one augmented heating region on the cavity floor near the trailing edge, and there is no augmented shear region predicted just upstream of the cavity leading edge. Due to the direct flow impingement on the downstream cavity wall, all pressure, heating and shear augmentations near the trailing edge are higher than those of the shallow cavity. All these observations are consistent with characterization of the deep cavity as an open cavity, as shown in Fig. 20b.

Finally, the challenges to validate these cavity predictions remain. Although infrared camera data were available for these tests, the image resolution was not sufficient to map out any qualitative flowfield features within these cavities.

G. Computational grids and estimated uncertainties

The two-dimensional axisymmetric and three-dimensional CFD computations of the H3 Mach 3.3 nozzle flowfields, including the test box and models, were performed using multi-block structured grids. All computational grids were generated using a commercial software package, *Pointwise* [28]. For the axisymmetric nozzle/test box simulations, 93,600 cells were used; the number of cells from the nozzle inlet to the end of the test box was 600, with 120 and 240 cells normal to the wall along the nozzle and the test box, respectively. For the three-dimensional nozzle/test box flowfields, the grid resolution was similar to the axisymmetric grids, and 4.67 million cells were used. For the 15° calibration wedge and standard TPS wedge models, the grid sizes were both 3.02 million cells, while the grid sizes used for the smooth and recessed shoulder feature wedge models were both 4.32 million cells. For simulations of the wedge model with two circular cavities, two separate simulations were performed, one for each cavity, with both grids having 7.99 million cells. Based on a limited number of grid refinement studies, grid quality issues of the computations and numerical accuracy are adequately addressed.

CFD computations of arc-jet flows, as for hypersonic flight simulations, include uncertainties in many of the model input parameters. It is not possible currently to do a complete uncertainty analysis of computed results for all the simulation input parameters. The most important input parameter of the arc-jet test flow is the total enthalpy and its distribution at the nozzle inlet. Noting that the centerline total enthalpies used in CFD simulations rely on the pitot pressure and the null-point probe sweep data, wedge calorimeter plate data, facility data, and other modeling input parameters, the uncertainty in the heat flux predictions for the smooth wedge models is estimated to be as much as ±20%, and the uncertainty in the surface pressure predictions is estimated to be ±5-10%. For the test articles with cavities, uncertainties in predicted surface pressure and heat flux, and their distributions are clearly larger, but they cannot be assessed at this time. Note that although the use of any turbulence models in turbulent CFD flow simulations increases the uncertainty in heat flux predictions, the comparisons of the computed results with the water-cooled calibration plate data, as have been used in the present paper and elsewhere, are important to establish these uncertainty estimates.

Uncertainty analyses of surface pressure and heat flux measurements are also not available. The pitot pressure and null-point calorimeter measurements as well as the wedge calibration plate pressure and heat flux measurements using coaxial thermocouples are standard AEDC H3 facility measurements [4, 7]. However, based on the authors' experience with historical NASA Ames arc-jet data and similar measurements, the heat flux measurements are estimated to be accurate to within ±15% and the pressure measurements to within ±5%. It should be noted that most of the Ames heat flux data were obtained with slug calorimeters [29], Gardon gage calorimeters [30], and some recently with the null-point and coaxial thermocouple heat flux gages [31, 32]. One of the important experimental challenges in arc-jet flow calibration is to obtain consistent heat flux measurements when multiple heat flux measuring devices (slug, Gardon, null-point and coaxial thermocouple gages) are used. Contributing factors are mostly due to calibration issues with the heat flux gages and methodologies to infer the heat flux from these measurement devices.

Calorimeters with a coaxial thermocouple and null-point calorimeters are also used at NASA Ames [31]. Although their estimated uncertainties [32] are similar to those of the slug measurements, they could be larger especially when the probe sizes are relatively small.

VI. Summary and Concluding Remarks

Computational simulations and analysis of arc-jet wedge tests conducted in the AEDC H3 facility Mach 3.3 nozzle are reported. The analysis comprises turbulent CFD simulations of the nonequilibrium flowfield in the facility nozzle, into the test box and over the wedge models, and comparisons with the experimental measurements. These simulations take into account non-uniform total enthalpy profiles at the nozzle inlet as well as the expansion waves emanating from the nozzle exit and their effects on the wedge model flowfields. The presented computational results are in good agreement with the facility calibration measurements (probe sweeps and calibration plate data). CFD simulations are then used to predict surface quantities for the wedge models tested, to assess the effects of the model shape change and test article recession, and to predict surface quantities for the test articles with two circular cavities.

These computational simulations provide estimates of the arc-jet test environment parameters that are not measured but are needed to evaluate the performance of TPS materials tested. Specifically, the CFD simulation results are used to estimate centerline total enthalpy of the test flow, hot wall heat flux and surface shear on the test articles, along with other boundary layer related parameters.

The presented CFD simulations of the H3 facility Mach 3.3 nozzle define arc-jet test environments for surface properties of TPS and provide a framework for tracing the TPS performance from this ground test facility to flight while assisting interpretation of the arc-jet data and future test planning, along with valuable insights into the arc-jet testing environment.

Acknowledgments

This work was funded by the NASA MSR-EES TPS project. The support from the NASA Ames Entry Systems and Technology Division, through contract NNA15BB15C to AMA, Inc., is gratefully acknowledged.

References

[1] Smith, D. M., Felderman, E. J., Shope, F. L., and Balboni, J. A., "Arc-Heated Facilities," *Advanced Hypersonic Test Facilities*, edited by F. K. Lu and D. E. Marren, AIAA Progress in Astronautics and Aeronautics, Vol. 198, American Institute of Aeronautics and Astronautics, Inc., Reston, VA, 2002, Chap. 10.

[2] Smith, D. M., and Felderman, J. E., "Aerothermal Testing of Space and Missile Materials in the Arnold Engineering Development Center Arc Jet Facilities," AIAA Paper 2006-3293, June 2006.

[3] "High-Enthalpy Arc-Heated Facilities at AEDC, Fact Sheet," Arnold Engineering Development Center, November 2023. https://www.arnold.af.mil/About-Us/Fact-Sheets/Display/Article/409285/high-enthalpy-arc-heated-facilities-at-aedc.

[4] Hammock, G., "Design and Calibration of the AEDC H3 Mach 3.0 High Heat Flux Nozzle," AIAA Paper 2014-2653, June 2014.

[5] ASTM E598-96, "Standard Test Method for Measuring Extreme Heat-Transfer Rates from High-Energy Environments Using a Transient, Null-Point Calorimeter," American Society for Testing and Materials, December 1996 (Reapproved 2002, originally published in 1977).

[6] Milos, F. S., Chen, Y.-K., and Mahzari, M. "Arcjet Tests and Thermal Response Analysis for Dual-Layer Woven Carbon Phenolic," *Journal of Spacecraft and Rockets*, Vol. 55, No. 3, May-June 2018, pp. 712-722.

[7] Smith, D. M., and Prabhu, D. K., "Flow Characterization and CFD Modeling of the AEDC H3 Mach 3.4 Freejet for Testing of Next-Generation NASA Planetary Probe TPS," National Space and Missile Materials Symposium paper, June 2014.

[8] Morgan, J. et al., "Arc-jet Testing of 3MDCP in Elevated Shear Environments for the Mars Sample Return - Earth Entry System," Extended abstract submitted for AIAA Aviation 2024 conferences, Nov. 2023.

[9] Wright, M. J., Candler, G. V., and Bose, D., "Data-Parallel Line Relaxation Method for the Navier-Stokes Equations," *AIAA Journal*, Vol. 36, No. 9, 1998, pp. 1603-1609.

[10] Wright, M. J., "Data-Parallel Line Relaxation Code, DPLR Version 4.02," Private Communication, June 2010.

[11] Park, C., *Nonequilibrium Hypersonic Aerothermodynamics*, John Wiley & Sons, Inc., New York, 1990, Chap. 4.

[12] Gökçen, T., Chen, Y. K., Skokova, K. A., and Milos, F. S., "Computational Analysis of Arc-Jet Stagnation Tests Including Ablation and Shape Change," *Journal of Thermophysics and Heat Transfer*, Vol. 24, No. 4, 2010, pp. 694-707; also, AIAA Paper 2009-3596, June 2009.

[13] Gökçen, T., "Effects of Test Box Pressure on Arc-Jet Flowfields and Implications for Testing," AIAA Paper 2018-3771, June 2018.

[14] Gökçen, T., and Alunni, A. I., "CFD Simulations of the IHF Arc-Jet Flow: 9-Inch Nozzle, Flow Surveys, LEAF Wedge Calibration Data," AIAA Paper 2019-3008, June 2019.

[15] Gökçen, T., "Analysis of Probe Surveys Conducted in the 10-MW TP3 Arc-Jet Facility 15-Inch Nozzle Flow," AIAA Paper 2021-3149, June 2021.

[16] Gökçen, T., Boghozian, T., and Alunni, A. I., "CFD Simulations of the IHF 13-Inch Nozzle Flow: 55° Sphere-Cone Model, Manufactured Fences and Gaps," AIAA Paper 2023-2427, January 2023.

[17] Spalart, P. R., and Allmaras, S. R., "A One-Equation Turbulence Model for Aerodynamic Flows," AIAA-92-0439, Jan. 1992.

[18] Spalart, P. R., and Allmaras, S. R., "A One-Equation Turbulence Model for Aerodynamic Flows," *Recherche Aerospatiale*, No. 1, 1994, pp. 5–21.

[19] Catris, S., and Aupoix, B., "Density Corrections for Turbulence Models," *Aerospace Science and Technology*, Vol. 4, No. 1, 2000, pp. 1–11.

[20] Menter, F. R., "Two-Equation Eddy-Viscosity Turbulence Models for Engineering Applications," *AIAA Journal*, Vol. 32, No. 8, Aug. 1994, pp. 1598-1605.

[21] Brown, J. L., "Turbulence Model Validation for Hypersonic Flows," AIAA Paper 2002-3308, June 2002.

[22] Baldwin, B. and Lomax, H., "Thin Layer Approximation and Algebraic Model for Separated Turbulent Flows," AIAA Paper 78-257, Jan. 1978.

[23] Brown, J. L., "Hypersonic Shock Wave Impingement on Turbulent Boundary Layers: Computational Analysis and Uncertainty," *Journal of Spacecraft and Rockets*, Vol. 50, No. 1, Jan-Feb. 2013, pp. 96–122; see also AIAA Paper 2011-3143.

[24] ASTM E341-96, "Standard Practice for Measuring Plasma Arc Gas Enthalpy by Energy Balance," American Society for Testing and Materials, December 1996 (Reapproved 2002).

[25] Gökçen, T., "CFD Results for AEDC H3 Mach 3.3 Nozzle Wedge Tests (Probe Sweeps, Calibration Plate Data, TPS Plate Wedge): HEEET Project Tests 2014-2016," MSR-EES TPS Working Group presentation, 1 March 2021.

[26] Everhart, J. E., "Supersonic/Hypersonic Laminar Heating Correlations for Rectangular and Impact-Induced Open and Closed Cavities," *Journal of Spacecraft and Rockets*, Vol. 46, No. 3, May-June 2009, pp. 545-560; see also AIAA Paper 2008-1283, Jan. 2008.

[27] Everhart, J. E., and Greene, F. A., "Turbulent Supersonic/Hypersonic Heating Correlations for Open and Closed Cavities," *Journal of Spacecraft and Rockets*, Vol. 47, No. 4, July–August 2010, pp. 545-554; see also AIAA Paper 2009-1400, Jan. 2009.

[28] "*Pointwise*, Version 18.4," Pointwise, Inc. of Cadence Design Systems, Fort Worth, TX.

[29] ASTM E457-96, "Standard Test Method for Measuring Heat-Transfer Rate Using a Thermal Capacitance (Slug) Calorimeter," American Society for Testing and Materials, Ocober 1996 (Reapproved 2002, originally published in 1972).

[30] ASTM E511-07, "Standard Test Method for Measuring Heat Flux Using a Copper-Constantan Circular Foil Heat-Flux Gage," American Society for Testing and Materials, December 2007 (original standard published in 1973).

[31] Terrazas-Salinas, I., Carballo, J. E., Driver, D. M., and Balboni, J. A., "Comparison of Heat Transfer Measurement Devices in Arc Jet Flows with Shear," AIAA Paper 2010-5053, June 2010.

[32] Driver, D. M., Philippidis, D., and Terrazas-Salinas, I., "Uncertainty Analysis of Coaxial Thermocouple Calorimeters used in Arc Jets," AIAA Paper 2018-3770, June 2018.